

NUMERICAL SHAPE OPTIMIZATION OF THE CANHAM-HELFRICH-EVANS BENDING ENERGY

MICHAEL NEUNTEUFEL, JOACHIM SCHÖBERL, AND KEVIN STURM

ABSTRACT. In this paper we propose a novel numerical scheme for the Canham–Helfrich–Evans bending energy based on a three-field lifting procedure of the distributional shape operator to an auxiliary mean curvature field. Together with its energetic conjugate scalar stress field as Lagrange multiplier the resulting fourth order problem is circumvented and reduced to a mixed saddle point problem involving only second order differential operators. Further, we derive its analytical first variation (also called first shape derivative), which is valid for arbitrary polynomial order, and discuss how the arising shape derivatives can be computed automatically in the finite element software NGSolve. We finish the paper with several numerical simulations showing the pertinence of the proposed scheme and method.

Keywords: Canham–Helfrich–Evans bending energy, shape optimization, mixed finite element method, distributional curvature, biomembrane.

MSC2020: 65N30, 65K10, 53E40, 49M05, 74K15

1. INTRODUCTION

In this paper we study the numerical minimization of the Canham–Helfrich–Evans [9, 21, 26] bending energy

$$\mathcal{W}(\partial\Omega) = 2\kappa_b \int_{\partial\Omega} (H - H_0)^2 ds, \quad \Omega \subset \mathbf{R}^3 \text{ bounded domain}, \quad (1.1)$$

subject to the following volume and area constraints

$$|\Omega| = V_0, \quad |\partial\Omega| = A_0, \quad (1.2)$$

where the positive constants $V_0, A_0 > 0$ obey the isoperimetric inequality

$$V_0 \leq \frac{A_0^{\frac{3}{2}}}{6\sqrt{\pi}}. \quad (1.3)$$

Here $H := \frac{1}{2}(\kappa_1 + \kappa_2)$ denotes the mean curvature of $\partial\Omega$, κ_1 and κ_2 its principle curvatures, $2H_0$ the so-called spontaneous curvature, and κ_b a bending elastic constant. Henceforth we will use the abbreviation $\mathcal{S} := \partial\Omega$ keeping in mind that \mathcal{S} is the surface enclosing the volume Ω . The Energy (1.1) was proposed to model membranes such as vesicles and red-blood cells [26, 37]. The numerical treatment of this problem is not straight-forward since the computation of the mean curvature typically involves the Laplace–Beltrami operator of the normal field, which would involve fourth order derivatives of the surface coordinates and thus requires a certain smoothness of the surface. Typically shapes are approximated with continuous, non-smooth triangulations (mostly linear or quadratic ones) leading to the fundamental and non-trivial question of computing/approximating the appropriate curvature. Nevertheless, several approaches to tackle this problem have been proposed. For a recent

comprehensive review of the Canham–Helfrich–Evans energy including various numerical approaches we refer to [25].

A variety of methods are based on the approximation of the Laplace–Beltrami operator by means of discrete differential geometry (DDG) [36, 24, 55]. The minimization is then achieved by e.g., differentiating the discrete energy with respect to the nodes and follow a negative gradient, see [3] for a comparison with several established numerical approximation schemes minimizing the Canham–Helfrich–Evans energy. A popular discretization scheme for the Laplace–Beltrami operator is the finite difference cotangent method on a Voronoi area entailing also a direct computation of a possibly involved Gaussian curvature in terms of the angle deficit, used e.g. in [4, 6, 48].

Beside boundary integral methods [42, 53, 22], procedures based on surface finite element methods (SFEM) [19, 20] approximate the surface of the shape with (possible high-order curved) isoperimetric elements. For linear triangulation the discrete normal vectors are sometimes averaged giving the possibility of computing the weak gradient globally [1]. For higher polynomial orders, however, the shape derivative yields complicated expressions due to the (nonlinear) averaging procedure.

Using smooth approximations of the surface by e.g. high-order B-splines or sub-division algorithms has been recently investigated in [43, 52], circumventing a non-continuous normal vector field.

Level set and phase field approaches [17, 35, 31] discretize the full space and the surface gets represented implicitly by a level set function. On the one hand geometric quantities as the normal vector are therefore easier accessible and changes of the shape’s topology are allowed, but on the other hand full-space computations have to be performed.

The shape derivative of geometric quantities and the full Canham–Helfrich–Evans energy has been computed e.g. in [10, 15, 30, 54] involving fourth order derivatives and the Gauss curvature of the shape. In [8] the mean curvature vector $\mathbf{H} = H\boldsymbol{\nu}$ is introduced as independent field and the equations are rewritten in such a way that no expressions in terms of the normal vector $\boldsymbol{\nu}$ in strict sense are left.

Mostly, instead of a quasi-static procedure a time-stepping algorithm with possible damping and stabilization techniques are used to find stationary solutions or for dynamic tests. For evolutionary geometries the famous time-stepping algorithm of Dziuk [18] is frequently considered, which has recently been further developed for mean curvature and Willmore flows in [28, 29], where - in contrast to Dziuk’s algorithm - convergence has been rigorously proven.

In this work, we propose a novel discretization approach based on a lifting procedure of the distributional (mean) curvature. Besides the classical element-wise shape operator, also the angle of the jump of the normal vector between two adjacent elements as taken as element-boundary integral such that the shape derivative can directly be applied. A derivation of the involved duality pairing is presented to build a bridge between (distributional based) surface finite elements and DDG, where several formulations rely also on the angle [24]. By introducing the scalar-valued mean curvature κ as independent unknown, in combination with the corresponding Lagrange multiplier σ the fourth order problem is avoided by introducing two second order problems. Further, the method also works for low-order polynomials on affine triangulation as well as for arbitrary polynomially curved elements without changing any term. The gradient based shape optimization algorithm is then applied to several well-established benchmark examples, where the stationary equilibrium shapes of the Canham–Helfrich–Evans energy, including possible spontaneous curvature, are computed.

The highlights of our paper are:

- novel numerical scheme to discretize the Canham–Helfrich–Evans bending energy based on a lifting of the distributional shape operator
- rigorous computation of first variation of the discretized bending energy
- numerical minimization of the bending energy using gradient-type algorithm using the first variation

2. NOTATION AND PROBLEM STATEMENT

In what follows, we will denote by \mathcal{S} a $d-1$ -dimensional closed submanifold in \mathbf{R}^d , $d = 2, 3$, and by $\Omega \subset \mathbf{R}^d$ the enclosed volume, i.e., $\mathcal{S} = \partial\Omega$ is the topological boundary of Ω . We say that a function $f : \mathcal{S} \rightarrow \mathbf{R}^d$ is k -times differentiable if there exists a neighborhood U of \mathcal{S} and a k -times differentiable function $\tilde{f} : \mathcal{S} \rightarrow \mathbf{R}^d$, such that, $\tilde{f} = f$ on \mathcal{S} . Given a differentiable function $f : \mathcal{S} \rightarrow \mathbf{R}^d$ and an extension \tilde{f} , we define the tangential Jacobian and gradient of a function $f : \mathcal{S} \rightarrow \mathbf{R}^d$ by

$$\partial^{\mathcal{S}} f := \partial \tilde{f} P_{\mathcal{S}}, \quad \nabla^{\mathcal{S}} f := P_{\mathcal{S}} \partial \tilde{f}^{\top}. \quad (2.1)$$

Here, $P_{\mathcal{S}} := \mathbf{I} - \boldsymbol{\nu} \otimes \boldsymbol{\nu} : \mathbf{R}^d \rightarrow T\mathcal{S} := \cup_{p \in \mathcal{S}} T_p \mathcal{S}$ denotes the projection onto the tangential space of \mathcal{S} , with $(\mathbf{a} \otimes \mathbf{b})\mathbf{c} := (\mathbf{b} \cdot \mathbf{c})\mathbf{a}$ for $\mathbf{a}, \mathbf{b}, \mathbf{c} \in \mathbf{R}^d$ being the outer product, and $\boldsymbol{\nu}$ denotes the outward pointing normal vector field along $\partial\Omega$. Further, we will neglect the subscript for the Euclidean norm $\|\cdot\|_2$ and denote in three dimensions the vector cross product by $\mathbf{a} \times \mathbf{b}$.

For the discretization, let \mathcal{T}_h be a piecewise smooth and globally continuous surface approximating \mathcal{S} . More precisely, let $\mathcal{T}_h = \{T_i\}_{i=1}^N$ with T_i smooth manifolds and piecewise smooth boundary ∂T and the vertices of \mathcal{T}_h lie on \mathcal{S} . We define $T\mathcal{T}_h := \cup_i T T_i$ as the discrete tangential space of \mathcal{T}_h . In 3D, on the edges we can define (normalized) tangential vectors $\boldsymbol{\tau}_L$ and $\boldsymbol{\tau}_R$ such that the co-normal (element-normal) vectors $\boldsymbol{\mu}_L := \boldsymbol{\nu}_L \times \boldsymbol{\tau}_L$ and $\boldsymbol{\mu}_R := \boldsymbol{\nu}_R \times \boldsymbol{\tau}_R$ are pointing outward of T_L and T_R , respectively, see Figure 2.1. We will neglect the subscripts L and R if the corresponding element T is obvious. Integrating over volume, boundary, or edges (vertices in 2D) is denoted by dx , ds , or $d\gamma$, respectively.

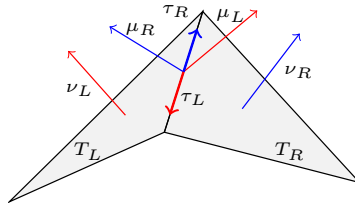


FIGURE 2.1. Normal, tangential, and co-normal (element-normal) vectors $\boldsymbol{\nu}$, $\boldsymbol{\tau}$, and $\boldsymbol{\mu}$ on two neighboured elements.

We incorporate the constraints (1.2) in a weak sense using a penalty formulation, with $c_A, c_V > 0$ denoting the penalty parameters:

$$\mathcal{J}(\mathcal{S}) = \mathcal{W}(\mathcal{S}) + \underbrace{c_A (|\mathcal{S}| - A_0)^2}_{=: J_{\text{surf}}(\mathcal{S})} + \underbrace{c_V (|\Omega| - V_0)^2}_{=: J_{\text{vol}}(\Omega)}. \quad (2.2)$$

Other approaches such as (augmented) Lagrangian [40] are also possible.

Later, in Section 5, we present a procedure to improve surface area preservation if the initial shape already has the desired area.

3. CURVATURE COMPUTATION

In this section we derive the discrete shape operator in terms of distributions, related to discrete differential geometry involving the angle of the normal vector jump between two adjacent elements. Then a variational formulation for computing the curvature is presented and further tailored to the problem of lifting only the mean curvature H instead of the full shape operator. Finally, the corresponding perturbed problem is derived as preparation for the shape derivatives in Section 4.

3.1. Discrete shape operator. Given the shape operator $-\partial^{\mathcal{S}}\boldsymbol{\nu} : TS \times TS \rightarrow \mathbf{R}$ on a smooth $d - 1$ -dimensional submanifold, the mean curvature H is computed by a $\frac{1}{2}$ times the trace of $-\partial^{\mathcal{S}}\boldsymbol{\nu}$, also called the Weingarten tensor,

$$H = -\frac{1}{2} \operatorname{tr}(\partial^{\mathcal{S}}\boldsymbol{\nu}). \quad (3.1)$$

Let now $\mathcal{T}_{h,k}$ be a triangulation of \mathcal{S} with polynomial approximation order $k \geq 1$. For procedures curving the mesh appropriately for optimal isoparametric finite element we refer to [33, 19]. In this work we use a projection-based interpolation procedure for curving geometries described in [13]. If the order of approximation is obvious, we will simply write \mathcal{T}_h . Given a triangulation, we define the skeleton $\mathcal{E}_{h,k}$ of $\mathcal{T}_{h,k}$ as the set of all edges or vertices of $\mathcal{T}_{h,k}$ in 3D or 2D, respectively. The set of all polynomials up to order $\ell \geq 0$ on the triangulation $\mathcal{T}_{h,\ell}$ and - in three dimensions - skeleton $\mathcal{E}_{h,\ell}$ is denoted by $\mathcal{P}^\ell(\mathcal{T}_h)$ and $\mathcal{P}^\ell(\mathcal{E}_h)$, respectively.

For an affine triangulation $\mathcal{T}_{h,1}$ the discrete outer normal vector $\boldsymbol{\nu}$ is constant on each facet of $\mathcal{T}_{h,1}$ (i.e., piecewise constant) and thus, $\partial^{\mathcal{S}}\boldsymbol{\nu}|_T = 0$ for all $T \in \mathcal{T}_{h,1}$. Moreover the normal vector may jump over the interfaces, see Figure 3.1. Hence, the shape operator, which we refer to as discrete shape operator, can at best be a distribution and will be defined below. Our definition is also motivated by discrete differential geometry, e.g. [24], where the angle is also used as part of the curvature computation.

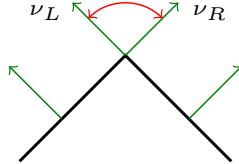


FIGURE 3.1. Jump of normal vector over two affine elements.

To illustrate the idea we start with an affine curve in two dimensions and without loss of generality consider two line segments and one point $\mathbf{P} = (0, 0)$, where the normal vector jumps with angle $\alpha > 0$ as depicted in Figure 3.2 (a). Our goal is to derive an approximation of the curvature formula at the point \mathbf{P} . To this end, we construct a family of C^1 -smooth approximation of the curve parameterized by $\varepsilon > 0$. Starting with an ε -circle centered at \mathbf{P} , we define the unique circle that goes through the same intersection points with the curve as the ε -circle and cuts it in a 90 degree angle, see Figure 3.2 (b). This circle with radius $r_\varepsilon = \varepsilon \frac{1+\cos(\alpha)}{\sin(\alpha)}$ and midpoint $\mathbf{M}_\varepsilon = (\varepsilon, -r_\varepsilon)$ is then used as C^1 -approximation of the junction, Figure 3.2 (c). Thus, we can define the continuous and piecewise smooth approximated normal vector $\boldsymbol{\nu}_\varepsilon : \mathcal{T}_\varepsilon \rightarrow \mathbb{S}^1$

$$\boldsymbol{\nu}_\varepsilon(\mathbf{x}) = \begin{cases} \boldsymbol{\nu}_L & \text{for } \mathbf{x} \in T_L, \\ \frac{\mathbf{x} - \mathbf{M}_\varepsilon}{\|\mathbf{x} - \mathbf{M}_\varepsilon\|} & \text{for } \mathbf{x} \in T_\varepsilon, \\ \boldsymbol{\nu}_R & \text{for } \mathbf{x} \in T_R. \end{cases} \quad (3.2)$$

Let us now calculate the shape operator of the regularized surface. We first notice that $\|\boldsymbol{\nu}_\varepsilon\| = 1$ and thus $\partial^S \boldsymbol{\nu}_\varepsilon = \partial \boldsymbol{\nu}_\varepsilon$. Therefore fixing \mathbf{x} near T_ε we compute the (i, j) entry of $\partial \boldsymbol{\nu}_\varepsilon(\mathbf{x})$, $\mathbf{x} \in T_\varepsilon$:

$$\partial_{x_i}(\boldsymbol{\nu}_\varepsilon)_j(\mathbf{x}) = \frac{1}{\|\mathbf{x} - \mathbf{M}_\varepsilon\|} \left(\delta_{ij} - \frac{1}{\|\mathbf{x} - \mathbf{M}_\varepsilon\|} ((\mathbf{x} - \mathbf{M}_\varepsilon) \cdot \mathbf{e}_i (\mathbf{x} - \mathbf{M}_\varepsilon) \cdot \mathbf{e}_j) \right), \quad (3.3)$$

where δ_{ij} denotes the Kronecker delta and \mathbf{e}_i the i th unit-vector, $\mathbf{e}_i(j) = \delta_{ij}$. This can equivalently be written as

$$\partial \boldsymbol{\nu}_\varepsilon(\mathbf{x}) = \frac{1}{r_\varepsilon} \boldsymbol{\mu}_\varepsilon \otimes \boldsymbol{\mu}_\varepsilon, \quad \boldsymbol{\mu}_\varepsilon := \frac{1}{r_\varepsilon} \begin{pmatrix} -(x_2 - M_{\varepsilon,2}) \\ x_1 - M_{\varepsilon,1} \end{pmatrix}, \quad (3.4)$$

where \mathbf{I}_2 denotes the identity matrix in two dimensions.

Note that $\boldsymbol{\mu}_\varepsilon = -\boldsymbol{\mu}_L$ and $\boldsymbol{\mu}_\varepsilon = \boldsymbol{\mu}_R$ on the interfaces $\overline{T}_\varepsilon \cap \overline{T}_L$ and $\overline{T}_\varepsilon \cap \overline{T}_R$, where $\boldsymbol{\mu}_L$ and $\boldsymbol{\mu}_R$ are the co-normal vectors, cf. Figure 2.1. Further, there exists a continuous and bijective mapping $\Phi_\varepsilon : \mathcal{T}_h \rightarrow \mathcal{T}_\varepsilon$ given by

$$\Phi_\varepsilon(\mathbf{x}) := \begin{cases} \mathbf{x} & \text{for } \mathbf{x} \in \mathcal{T}_h \setminus U_\varepsilon(\mathbf{P}), \\ \frac{r_\varepsilon}{\|\mathbf{x} - \mathbf{M}_\varepsilon\|} (\mathbf{x} - \mathbf{M}_\varepsilon) & \text{for } \mathbf{x} \in \mathcal{T}_h \cap U_\varepsilon(\mathbf{P}), \end{cases} \quad (3.5)$$

with $\Phi_\varepsilon \xrightarrow{\varepsilon \rightarrow 0} \text{Id}$.

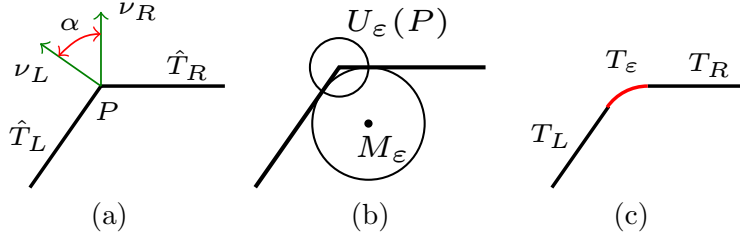


FIGURE 3.2. Construction of approximation of discrete jump. (a) The affine curve with jump angle α . (b) The construction of the circles. (c) The final approximated smooth curve.

To compute the limit $\varepsilon \rightarrow 0$ we define the corresponding test function on the triangulation $\boldsymbol{\Psi} : T\mathcal{T}_h \times T\mathcal{T}_h \rightarrow \mathbf{R}$ to be co-normal co-normal continuous, i.e., $\boldsymbol{\Psi}_{\boldsymbol{\mu}_L \boldsymbol{\mu}_L} := \boldsymbol{\mu}_L^\top \boldsymbol{\Psi}|_{T_L} \boldsymbol{\mu}_L = \boldsymbol{\mu}_R^\top \boldsymbol{\Psi}|_{T_R} \boldsymbol{\mu}_R =: \boldsymbol{\Psi}_{\boldsymbol{\mu}_R \boldsymbol{\mu}_R}$ on the skeleton \mathcal{E}_h . Thus, the co-normal co-normal component does not “see” the junction of the discretized geometry. Further it should be symmetric, as the shape operator is, and thus, is of the form $\boldsymbol{\Psi} = \Psi \boldsymbol{\mu} \otimes \boldsymbol{\mu}$ with $\Psi : \mathbf{R}^2 \rightarrow \mathbf{R}$ a continuous function. The test function on the smoothed surface $\mathcal{T}_\varepsilon = \Phi_\varepsilon(\mathcal{T}_h)$ reads $\boldsymbol{\Psi}_\varepsilon = \Psi \circ \Phi_\varepsilon^{-1} \boldsymbol{\mu}_\varepsilon \otimes \boldsymbol{\mu}_\varepsilon$. Then, in view of $\lim_{\varepsilon \searrow 0} \mathbf{M}_\varepsilon = \mathbf{P}$ and $\lim_{\varepsilon \searrow 0} r_\varepsilon = 0$, a change of variables, and Lebesgue dominated convergence Theorem yield

$$\begin{aligned} \langle -\partial^S \boldsymbol{\nu}, \boldsymbol{\Psi} \rangle_{\mathcal{T}_{h,1}} &:= \lim_{\varepsilon \rightarrow 0} (-\partial^S \boldsymbol{\nu}_\varepsilon, \boldsymbol{\Psi}_\varepsilon)_{L^2(\mathcal{T}_\varepsilon)} \\ &\stackrel{(3.4)}{=} \lim_{\varepsilon \rightarrow 0} \int_{\Gamma_\varepsilon = \Phi_\varepsilon(\Gamma_1)} -\frac{1}{r_\varepsilon} \boldsymbol{\mu}_\varepsilon \otimes \boldsymbol{\mu}_\varepsilon : \Psi \circ \Phi_\varepsilon^{-1} \boldsymbol{\mu}_\varepsilon \otimes \boldsymbol{\mu}_\varepsilon \, ds \\ &= \lim_{\varepsilon \rightarrow 0} \int_{\Gamma_1} -\Psi(\mathbf{M}_\varepsilon + r_\varepsilon \mathbf{x}) \, ds = -\underbrace{|\Gamma_1|}_{=\alpha} \Psi(\mathbf{P}) \\ &= - \int_{\mathbf{P}} \angle(\boldsymbol{\nu}_L, \boldsymbol{\nu}_R) \Psi \, d\gamma, \end{aligned}$$

with the notation $\angle(\boldsymbol{\nu}_L, \boldsymbol{\nu}_R) := \arccos(\boldsymbol{\nu}_L \cdot \boldsymbol{\nu}_R)$ and

$$\Gamma_\varepsilon := \left\{ \mathbf{M}_\varepsilon + r_\varepsilon \begin{pmatrix} \cos(s) \\ \sin(s) \end{pmatrix}, s \in \left(\frac{\pi}{2}, \frac{\pi}{2} + \alpha\right) \right\}, \quad \Gamma_1 := \left\{ \begin{pmatrix} \cos(s) \\ \sin(s) \end{pmatrix}, s \in \left(\frac{\pi}{2}, \frac{\pi}{2} + \alpha\right) \right\}. \quad (3.6)$$

Thus, the discrete shape operator on a triangulation $\mathcal{T}_{h,k}$ can be defined as

$$\langle -\partial^S \boldsymbol{\nu}, \boldsymbol{\Psi} \rangle_{\mathcal{T}_{h,k}} := - \sum_{T \in \mathcal{T}_h} \int_T \partial^S \boldsymbol{\nu}|_T : \boldsymbol{\Psi} \, ds - \sum_{E \in \mathcal{E}_h} \int_E \angle(\boldsymbol{\nu}_L, \boldsymbol{\nu}_R) \boldsymbol{\Psi}_{\boldsymbol{\mu}\boldsymbol{\mu}} \, d\gamma, \quad (3.7)$$

for all $\boldsymbol{\Psi} \in \{\boldsymbol{\Psi} \boldsymbol{\mu} \otimes \boldsymbol{\mu}, : \boldsymbol{\Psi} : \mathcal{S} \rightarrow \mathbf{R} \text{ continuous}\}$. Note, that for a high order approximation of the surface the jump term becomes less important in terms of curvature information, however, it will be crucial for numerical stability. The derivation in the affine case can be related to Steiner's offset formula [51], where the surface is shifted along the discrete normal vector. Then, depending on how the appearing gap between the elements is filled, different expressions in terms of the angle are gained [2].



FIGURE 3.3. Construction of approximation of discrete jump in 3D. (a) The affine curve with junction. (b) The approximated smooth surface.

The generalization to two-dimensional sub-manifolds in three dimensions is done in an analogous manner, compare Figure 3.3. The vertices can be treated by an ε -sphere, compute the shape operator, and take the limit $\varepsilon \rightarrow 0$. However, as the regularized shape operator is of order $\mathcal{O}(\varepsilon^{-1})$ whereas the surface is of $\mathcal{O}(\varepsilon^2)$ the limit is zero.

Therefore, analogously to the two-dimensional case, the test function $\boldsymbol{\Psi} : \mathcal{T}_h \rightarrow \mathbf{R}_{\text{sym}}^{3 \times 3}, \mathbf{R}_{\text{sym}}^{3 \times 3}$ denoting the set of all 3×3 symmetric matrices, has to be co-normal co-normal continuous. The jump over element interfaces is denoted by $\llbracket \boldsymbol{\Psi}_{\boldsymbol{\mu}\boldsymbol{\mu}} \rrbracket$ and the space of symmetric co-normal co-normal continuous matrices acting on the tangent space is given by the Hellan–Herrmann–Johnson (HHJ) finite element space, see [11] and therein references, mapped on the surface

$$M_h^k(\mathcal{T}_h) := \{\boldsymbol{\sigma}_h \in [\mathcal{P}^k(\mathcal{T}_h)]_{\text{sym}}^{3 \times 3} : \llbracket \boldsymbol{\sigma}_{h,\boldsymbol{\mu}\boldsymbol{\mu}} \rrbracket = 0, \boldsymbol{\sigma}_h \boldsymbol{\nu} = \boldsymbol{\nu}^\top \boldsymbol{\sigma}_h = 0\}. \quad (3.8)$$

To construct such a finite element space one can start in the flat two-dimensional case and then map the resulting elements onto the surface by using the so-called Piola transformation to preserve the normal-normal continuity, we refer to [49] for an explicit construction and additional properties. We emphasize that the finite element space is related to the function space

$$H(\text{div div}, \mathcal{S}) := \{\boldsymbol{\sigma} \in [L^2(\mathcal{S})]_{\text{sym}}^{3 \times 3} : \text{div}^S(\text{div}^S(\boldsymbol{\sigma})) \in H^{-1}(\mathcal{S}), \boldsymbol{\sigma} \boldsymbol{\nu} = \boldsymbol{\nu}^\top \boldsymbol{\sigma} = 0\}, \quad (3.9)$$

where $H^{-1}(\mathcal{S})$ denotes for closed surfaces \mathcal{S} the topological dual space of $H^1(\mathcal{S}) := \{u \in L^2(\mathcal{S}) : \partial^S u \in [L^2(\mathcal{S})]^3\}$.

As will be discussed in the following subsections, the matrix valued curvature tensor is going to be reduced to a scalar quantity representing the mean curvature and thus, we do not get into further details with respect to matrix valued spaces.

3.2. Variational formulation. The corresponding variational problem for (3.7) computing the discrete Weingarten tensor κ reads: Find $\kappa \in M_h^k(\mathcal{T}_h)$ such that for all $\delta\kappa \in M_h^k(\mathcal{T}_h)$

$$\int_{\mathcal{T}_h} \kappa : \delta\kappa \, ds = - \sum_{T \in \mathcal{T}_h} \int_T \partial^S \nu : \delta\kappa \, ds - \sum_{E \in \mathcal{E}_h} \int_E \triangleleft(\nu_L, \nu_R) \delta\kappa_{\mu\mu} \, d\gamma. \quad (3.10)$$

As discussed in [39, 38] by introducing the averaged normal vector $\{\nu\} := \frac{\nu_L + \nu_R}{\|\nu_L + \nu_R\|}$ the jump terms can be reordered yielding

$$\begin{aligned} \int_{\mathcal{T}_h} \kappa : \delta\kappa \, ds &= - \sum_{T \in \mathcal{T}_h} \left(\int_T \partial^S \nu : \delta\kappa \, ds + \int_{\partial T} \triangleleft(\nu, \{\nu\}) \delta\kappa_{\mu\mu} \, d\gamma \right) \\ &= - \sum_{T \in \mathcal{T}_h} \left(\int_T \partial^S \nu : \delta\kappa \, ds + \int_{\partial T} \left(\frac{\pi}{2} - \triangleleft(\mu, \{\nu\}) \right) \delta\kappa_{\mu\mu} \, d\gamma \right), \end{aligned} \quad (3.11)$$

where the latter is numerically more stable as the derivative of $\arccos(x)$ has a singularity at $x = 1$ and we expect the shapes to be close of being smooth.

With this preliminary work, the minimization problem together with the constraints (2.2) can be described by the Lagrange functional

$$\begin{aligned} \mathcal{L}(\mathcal{T}_h, \kappa, \sigma) &:= \sum_{T \in \mathcal{T}_h} \left(\int_T 2\kappa_b \left(\frac{1}{2} \text{tr}(\kappa) - H_0 \right)^2 + (\kappa + \partial^S \nu) : \sigma \, ds \right. \\ &\quad \left. + \int_{\partial T} \left(\frac{\pi}{2} - \triangleleft(\mu, \{\nu\}) \right) \sigma_{\mu\mu} \, d\gamma \right) \\ &\quad + c_A J_{\text{surf}}(\mathcal{T}_h) + c_V J_{\text{vol}}(\mathcal{T}_h), \end{aligned} \quad (3.12)$$

where σ is the Lagrange multiplier forcing the “lifting” $\kappa = -\nabla^S \nu$ having the physical meaning of a moment tensor. Lagrangian (3.12) can be seen as a three-field formulation involving the shape (or equivalently the displacement), the independent shape operator field κ , and the moment tensor σ . As discussed in the following section, the formulation can be reduced as only the trace of κ will enter the bending energy of the shape. Therefore there is no need to lift the whole shape operator $-\partial^S \nu$.

3.3. Reduction for mean curvature. In (3.12) the full shape operator $-\partial^S \nu$ is lifted to κ via the Lagrange parameter σ . However, only the trace, $\text{tr}(\kappa)$, is involved in the final energy. Thus, we would “waste” computational effort lifting the deviatoric part of $-\partial^S \nu$. Further, using the lowest order HHJ elements $M_h^0(\mathcal{T}_h)$ (3.8) its trace is only a constant per element yielding a huge kernel. Therefore, deformations of the shape can occur producing mean curvature but lying in the kernel of the trace of κ yielding a non-robust formulation.

With this motivation, we adapt (3.12) by additionally enforcing that the deviatoric part of κ has to be zero. Further, to guarantee the Ladyzhenskaya–Babuška–Brezzi (LBB) condition for saddle-point problems also the deviatoric part of σ is assumed zero, which is a logical consequence as only the trace of the shape operator $-\partial^S \nu$ needs to be lifted to κ .

The deviatoric-free field κ is one-dimensional and of the form $\kappa = \kappa \mathbf{P}_S$ with $\kappa : \mathcal{S} \rightarrow \mathbf{R}$. Further, due to the co-normal co-normal continuity of κ we deduce that with $\kappa_{\mu\mu} = \mu^\top (\kappa \mathbf{P}_S) \mu = \kappa$ the reduced field κ is continuous and thus in $H^1(\mathcal{S})$. With the H^1 -conforming Lagrangian finite element space

$$V_h^k(\mathcal{T}_h) := \{u \in \mathcal{P}^k(\mathcal{T}_h) : u \text{ continuous on } \mathcal{T}_h\} \subset H^1(\mathcal{S}). \quad (3.13)$$

the reduced curvature problem reads: find $\kappa \in V_h^k(\mathcal{T}_h)$ such that for all $\delta\kappa \in V_h^k(\mathcal{T}_h)$

$$\int_{\mathcal{T}_h} \kappa \delta\kappa ds = - \sum_{T \in \mathcal{T}_h} \left(\int_T \text{tr}(\partial^S \boldsymbol{\nu}) \delta\kappa ds + \int_{\partial T} \left(\frac{\pi}{2} - \angle(\boldsymbol{\mu}, \{\boldsymbol{\nu}\}) \right) \delta\kappa d\gamma \right). \quad (3.14)$$

With the same arguments for σ the reduced final Lagrangian reads for $\kappa, \sigma \in V_h^k(\mathcal{T}_h)$

$$\begin{aligned} \mathcal{L}(\mathcal{T}_h, \kappa, \sigma) := & \sum_{T \in \mathcal{T}_h} \left(\int_T 2\kappa_b \left(\frac{1}{2}\kappa - H_0 \right)^2 + (\kappa + \text{tr}(\partial^S \boldsymbol{\nu}))\sigma ds + \int_{\partial T} \left(\frac{\pi}{2} - \angle(\boldsymbol{\mu}, \{\boldsymbol{\nu}\}) \right) \sigma d\gamma \right) \\ & + c_A J_{\text{surf}}(\mathcal{T}_h) + c_V J_{\text{vol}}(\mathcal{T}_h). \end{aligned} \quad (3.15)$$

We note, that also in [8] the mean curvature has been added as additional unknown. Therein, however, the mean curvature vector $\mathbf{H} = \kappa \boldsymbol{\nu}$ has been considered to eliminate all terms involving the normal vector $\boldsymbol{\nu}$. In this work we still use the normal vector and the additionally involved quantities κ and σ are only scalar-valued.

In Section 4 we will discuss the shape derivative of (3.15). These computations are not straight forward due to the non-standard jump term.

3.4. Perturbed problem. As preparation for the shape derivatives, we will now introduce perturbations of the triangulation \mathcal{T}_h using vector fields $\mathbf{X} \in W_\infty^1(\mathbf{R}^d)^d$, where $W_\infty^1(\mathbf{R}^d)^d$ denotes the space of Lipschitz continuous functions, which will be discretized with H^1 -conforming finite elements. Further, we will focus on the three-dimensional case, the two-dimensional one follows the same lines. In the following let $\mathbf{X} \in [V_h^k(\mathcal{T}_h)]^3$, $k \geq 1$, be a vector field. Then we consider (3.14) on the family of perturbed domains:

$$\mathcal{T}_h^t := \{\mathbf{T}_t(T) : T \in \mathcal{T}_h\}, \quad \mathbf{T}_t(\mathbf{x}) = \mathbf{x} + t\mathbf{X}(\mathbf{x}), \quad \mathbf{x} \in \mathcal{T}_h, \quad \text{for } t \geq 0 \text{ small.}$$

Find $\kappa_t \in V_h(\mathcal{T}_h^t)$, such that

$$\int_{\mathcal{T}_h^t} \kappa_t \delta\kappa_t ds = - \sum_{T \in \mathcal{T}_h^t} \left(\int_T \text{tr}(\partial^{S_t} \boldsymbol{\nu}_t) \delta\kappa_t ds + \int_{\partial T} \left(\frac{\pi}{2} - \angle(\boldsymbol{\mu}_t, \{\boldsymbol{\nu}_t\}) \right) \delta\kappa_t d\gamma \right) \quad (3.16)$$

for all $\delta\kappa_t \in V_h(\mathcal{T}_h^t)$.

To compute the perturbed averaged normal vector $\{\boldsymbol{\nu}\}_t$ information of two neighboured elements are required at once. Under the assumption that the perturbation is “small enough” instead of measuring the angle with the perturbed averaged normal vector $\{\boldsymbol{\nu}\}_t$, we can use the unperturbed one, compare Figure 3.4. In three dimensions, however, one has to project $\{\boldsymbol{\nu}\} \circ \mathbf{T}_t^{-1}$ to the plane orthogonal to the perturbed tangent vector $\boldsymbol{\tau}_t$ and renormalize it to measure the correct angle

$$\mathbf{P}_{\boldsymbol{\tau}_t}^\perp(\{\boldsymbol{\nu}\}) := \frac{\{\boldsymbol{\nu}\} \circ \mathbf{T}_t^{-1} - (\{\boldsymbol{\nu}\} \circ \mathbf{T}_t^{-1} \cdot \boldsymbol{\tau}_t) \boldsymbol{\tau}_t}{\| \{\boldsymbol{\nu}\} \circ \mathbf{T}_t^{-1} - (\{\boldsymbol{\nu}\} \circ \mathbf{T}_t^{-1} \cdot \boldsymbol{\tau}_t) \boldsymbol{\tau}_t \|}. \quad (3.17)$$

A simple example for demonstrating the necessity of projection (3.17) is given as follows: if the two elements rotate by \mathbf{T}_t around the axis $\{\boldsymbol{\nu}\} \times \boldsymbol{\tau}_L$ then with $\angle(\boldsymbol{\mu}_t, \{\boldsymbol{\nu}\})$ a too small angle is measured from both sides indicating a wrong change of curvature.

Therefore, (3.16) changes to

$$\int_{\mathcal{T}_h^t} \kappa_t \delta\kappa_t ds = - \sum_{T \in \mathcal{T}_h^t} \left(\int_T \text{tr}(\partial^{S_t} \boldsymbol{\nu}_t) \delta\kappa_t ds + \int_{\partial T} \left(\frac{\pi}{2} - \angle(\boldsymbol{\mu}_t, \mathbf{P}_{\boldsymbol{\tau}_t}^\perp(\{\boldsymbol{\nu}\})) \right) \delta\kappa_t d\gamma \right) \quad (3.18)$$

for all $\delta\kappa_t \in V_h(\mathcal{T}_h^t)$.

A rigorous proof of the equivalence of (3.16) and (3.18) is provided by the following lemma.

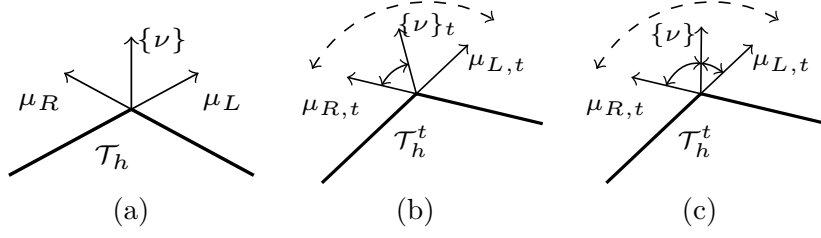


FIGURE 3.4. Angle computation. (a) Unperturbed surface. (b) Perturbed averaged normal vector on perturbed surface. (c) Unperturbed averaged normal vector on perturbed surface.

Lemma 3.1. *There holds*

$$\sum_{T \in \mathcal{T}_h^t} \int_{\partial T} \angle(\boldsymbol{\mu}_t, \{\boldsymbol{\nu}\}_t) d\gamma = \sum_{T \in \mathcal{T}_h^t} \int_{\partial T} \angle(\boldsymbol{\mu}_t, \mathbf{P}_{\boldsymbol{\tau}_t}^\perp(\{\boldsymbol{\nu}\})) d\gamma. \quad (3.19)$$

Proof. First, we rewrite the left and right hand side in (3.19) as sum over edges

$$\begin{aligned} \sum_{T \in \mathcal{T}_h^t} \int_{\partial T} \angle(\boldsymbol{\mu}_t, \{\boldsymbol{\nu}\}_t) d\gamma &= \sum_{E \in \mathcal{E}_h^t} \int_E \angle(\boldsymbol{\mu}_{L,t}, \{\boldsymbol{\nu}\}_t) + \angle(\boldsymbol{\mu}_{R,t}, \{\boldsymbol{\nu}\}_t) d\gamma, \\ \sum_{T \in \mathcal{T}_h^t} \int_{\partial T} \angle(\boldsymbol{\mu}_t, \mathbf{P}_{\boldsymbol{\tau}_t}^\perp(\{\boldsymbol{\nu}\})) d\gamma &= \sum_{E \in \mathcal{E}_h^t} \int_E \angle(\boldsymbol{\mu}_{L,t}, \mathbf{P}_{\boldsymbol{\tau}_t}^\perp(\{\boldsymbol{\nu}\})) + \angle(\boldsymbol{\mu}_{R,t}, \mathbf{P}_{\boldsymbol{\tau}_t}^\perp(\{\boldsymbol{\nu}\})) d\gamma. \end{aligned}$$

Note that $\{\boldsymbol{\nu}\}_t$ and $\mathbf{P}_{\boldsymbol{\tau}_t}^\perp(\{\boldsymbol{\nu}\})$ are single valued on E . Now, it is sufficient to prove that for all edges $E \in \mathcal{E}_h^t$

$$\int_E \angle(\boldsymbol{\mu}_{L,t}, \{\boldsymbol{\nu}\}_t) + \angle(\boldsymbol{\mu}_{R,t}, \{\boldsymbol{\nu}\}_t) d\gamma = \int_E \angle(\boldsymbol{\mu}_{L,t}, \mathbf{P}_{\boldsymbol{\tau}_t}^\perp(\{\boldsymbol{\nu}\})) + \angle(\boldsymbol{\mu}_{R,t}, \mathbf{P}_{\boldsymbol{\tau}_t}^\perp(\{\boldsymbol{\nu}\})) d\gamma. \quad (3.20)$$

We start with the left side. Noting that (compare Figure 2.1)

$$\boldsymbol{\mu}_{L,t} \perp \boldsymbol{\tau}_{L,t} = -\boldsymbol{\tau}_{R,t} \perp \boldsymbol{\mu}_{R,t}, \quad \boldsymbol{\nu}_{L,t} \perp \boldsymbol{\tau}_{L,t} = -\boldsymbol{\tau}_{R,t} \perp \boldsymbol{\nu}_{R,t}$$

and thus $\{\boldsymbol{\nu}\}_t \perp \boldsymbol{\tau}_{L,t}, \boldsymbol{\tau}_{R,t}$ and for sufficiently small perturbations $\dim(\text{span}\{\boldsymbol{\mu}_{L,t}, \boldsymbol{\mu}_{R,t}\}) = 2$ we get

$$\{\boldsymbol{\nu}\}_t \in \text{span}\{\boldsymbol{\mu}_{L,t}, \boldsymbol{\mu}_{R,t}\}.$$

Further $\{\boldsymbol{\nu}\}_t$ is normalized by construction and (for fine enough grids and small enough perturbations, compare Figure 2.1 and Figure 3.4) there exists an $\alpha \in [0, 1]$ such that $\{\boldsymbol{\nu}\}_t \in \text{span}\{\alpha \boldsymbol{\mu}_{L,t} + (1 - \alpha) \boldsymbol{\mu}_{R,t}\}$. Thus, the requirements of Lemma B.1 are fulfilled and we have

$$\angle(\boldsymbol{\mu}_{L,t}, \{\boldsymbol{\nu}\}_t) + \angle(\boldsymbol{\mu}_{R,t}, \{\boldsymbol{\nu}\}_t) = \angle(\boldsymbol{\mu}_{L,t}, \boldsymbol{\mu}_{R,t}).$$

For the right side of (3.20) we already showed $\boldsymbol{\mu}_{R,t}, \boldsymbol{\mu}_{L,t} \perp \boldsymbol{\tau}_t$ and $\dim(\text{span}\{\boldsymbol{\mu}_{L,t}, \boldsymbol{\mu}_{R,t}\}) = 2$. By construction of the projected averaged normal vector we further have

$$\|\mathbf{P}_{\boldsymbol{\tau}_t}^\perp(\{\boldsymbol{\nu}\})\| = 1, \quad \mathbf{P}_{\boldsymbol{\tau}_t}^\perp(\{\boldsymbol{\nu}\}) \perp \boldsymbol{\tau}_t$$

and thus, under the assumption that the perturbation is small enough, we have with the same argument as before that

$$\angle(\boldsymbol{\mu}_{L,t}, \mathbf{P}_{\boldsymbol{\tau}_t}^\perp(\{\boldsymbol{\nu}\})) + \angle(\boldsymbol{\mu}_{R,t}, \mathbf{P}_{\boldsymbol{\tau}_t}^\perp(\{\boldsymbol{\nu}\})) = \angle(\boldsymbol{\mu}_{L,t}, \boldsymbol{\mu}_{R,t})$$

and by transitivity

$$\angle(\boldsymbol{\mu}_{L,t}, \mathbf{P}_{\boldsymbol{\tau}_t}^\perp(\{\boldsymbol{\nu}\})) + \angle(\boldsymbol{\mu}_{R,t}, \mathbf{P}_{\boldsymbol{\tau}_t}^\perp(\{\boldsymbol{\nu}\})) = \angle(\boldsymbol{\mu}_{L,t}, \{\boldsymbol{\nu}\}_t) + \angle(\boldsymbol{\mu}_{R,t}, \{\boldsymbol{\nu}\}_t),$$

which finishes the proof. \square

We will see that the projection $\mathbf{P}_{\tau_t}^\perp(\cdot)$ does not induce a term in the first shape derivative, compare Lemma 4.5. Therefore one could neglect it if a gradient based algorithm is applied to solve the problem numerically. For a shape Newton algorithm, where additionally the second shape derivative is involved, however, the projection induces additional terms and thus, for sake of completeness, is kept in the following.

Before transforming the perturbed geometric quantities back to the initial shape \mathcal{T}_h we define the following basic properties. Let $\Phi : \hat{\mathcal{S}} \rightarrow \mathcal{S}$ be a mapping between two manifolds. For scalar functions $f : \mathcal{S} \rightarrow \mathbf{R}$ we have the chain rule

$$\nabla^{\mathcal{S}} f \circ \Phi = \mathbf{A} \nabla^{\hat{\mathcal{S}}} (f \circ \Phi), \quad \mathbf{A} := \left(\mathbf{I} - \frac{\partial \Phi^{-\top} \boldsymbol{\nu}}{|\partial \Phi^{-\top} \boldsymbol{\nu}|} \otimes \frac{\partial \Phi^{-\top} \boldsymbol{\nu}}{|\partial \Phi^{-\top} \boldsymbol{\nu}|} \right) \partial \Phi^{-\top} \quad (3.21)$$

and for a vector valued function $f : \mathcal{S} \rightarrow \mathbf{R}^3$

$$\partial^{\mathcal{S}} f \circ \Phi = \partial^{\hat{\mathcal{S}}} (f \circ \Phi) \mathbf{A}^\top. \quad (3.22)$$

Further, with $\mathcal{S}_t = \mathbf{T}_t(\mathcal{S})$, $\mathbf{T}_t(x) := x + t\mathbf{X}$, $\mathbf{X} \in C_c^1(\mathbf{R}^3)^3$, there holds

$$\mathbf{A}^\top(t) = \partial \mathbf{T}_t^{-1} \left(\mathbf{I} - \frac{\partial \mathbf{T}_t^{-\top} \boldsymbol{\nu}}{\|\partial \mathbf{T}_t^{-\top} \boldsymbol{\nu}\|} \otimes \frac{\partial \mathbf{T}_t^{-\top} \boldsymbol{\nu}}{\|\partial \mathbf{T}_t^{-\top} \boldsymbol{\nu}\|} \right), \quad \mathbf{A}^\top(0) = \mathbf{I} - \boldsymbol{\nu} \otimes \boldsymbol{\nu} \quad (3.23)$$

and

$$\begin{aligned} (\mathbf{A}^\top)'(0) &= -\partial \mathbf{X} (\mathbf{I} - \boldsymbol{\nu} \otimes \boldsymbol{\nu}) + \partial^{\mathcal{S}} \mathbf{X}^\top \boldsymbol{\nu} \otimes \boldsymbol{\nu} + \boldsymbol{\nu} \otimes \partial^{\mathcal{S}} \mathbf{X}^\top \boldsymbol{\nu} \\ &= -\partial^{\mathcal{S}} \mathbf{X} + 2 \operatorname{Sym}(\boldsymbol{\nu} \otimes \boldsymbol{\nu} \partial^{\mathcal{S}} \mathbf{X}). \end{aligned} \quad (3.24)$$

Here, $C^1(\mathbf{R}^d)$ denotes the set of continuous differentiable functions $f : \mathbf{R}^d \rightarrow \mathbf{R}$ and $C_c^1(\mathbf{R}^d)$ the set of continuous differentiable functions with compact support.

Next, we define element-wise the transformation determinants

$$w_t := \det(\partial \mathbf{T}_t) \|\partial \mathbf{T}_t^{-\top} \boldsymbol{\nu}\| \quad \text{and} \quad w_t^E := \|\partial \mathbf{T}_t \boldsymbol{\tau}\|. \quad (3.25)$$

It is readily checked that we have on the initial triangulation \mathcal{T}_h

$$\boldsymbol{\tau}^t := \boldsymbol{\tau}_t \circ \mathbf{T}_t = \frac{\partial \mathbf{T}_t \boldsymbol{\tau}}{\|\partial \mathbf{T}_t \boldsymbol{\tau}\|} \quad \text{and} \quad \boldsymbol{\nu}^t := \boldsymbol{\nu}_t \circ \mathbf{T}_t = \frac{\partial \mathbf{T}_t^{-\top} \boldsymbol{\nu}}{\|\partial \mathbf{T}_t^{-\top} \boldsymbol{\nu}\|}. \quad (3.26)$$

We define $\boldsymbol{\mu}^t := \boldsymbol{\nu}^t \times \boldsymbol{\tau}^t$ and can use (3.26) for the pull-back of $\boldsymbol{\mu}^t$. However, there exists a more compact form:

Lemma 3.2. *With $\mathbf{A}(t) := (\mathbf{I} - \boldsymbol{\nu}^t \otimes \boldsymbol{\nu}^t) \partial \mathbf{T}_t^{-\top}$ we have for $t \geq 0$,*

$$\boldsymbol{\mu}^t := \boldsymbol{\mu}_t \circ \mathbf{T}_t = \frac{\mathbf{A}(t) \boldsymbol{\mu}}{\|\mathbf{A}(t) \boldsymbol{\mu}\|}. \quad (3.27)$$

Proof. We compute using the formulas (3.26) for $\boldsymbol{\nu}^t$ and $\boldsymbol{\tau}^t$:

$$\begin{aligned} \boldsymbol{\mu}^t \cdot \boldsymbol{\nu}^t &= \frac{\partial \mathbf{T}_t^{-\top} \boldsymbol{\mu}}{\|\mathbf{A}(t) \boldsymbol{\mu}\|} \cdot (\mathbf{I} - \boldsymbol{\nu}^t \otimes \boldsymbol{\nu}^t) \boldsymbol{\nu}^t = 0, \\ \boldsymbol{\mu}^t \cdot \boldsymbol{\tau}^t &= \frac{\partial \mathbf{T}_t^{-\top} \boldsymbol{\mu}}{\|\mathbf{A}(t) \boldsymbol{\mu}\|} \cdot (\mathbf{I} - \boldsymbol{\nu}^t \otimes \boldsymbol{\nu}^t) \boldsymbol{\tau}^t = \frac{1}{\|\mathbf{A}(t) \boldsymbol{\mu}\| \|\partial \mathbf{T}_t \boldsymbol{\tau}\|} \boldsymbol{\mu} \cdot \boldsymbol{\tau} = 0. \end{aligned}$$

Therefore $\boldsymbol{\mu}^t$ lies in $\text{span}\{\boldsymbol{\nu}^t, \boldsymbol{\tau}^t\}^\perp = \text{span}\{\boldsymbol{\mu}^t\}$ and thus $\det(\boldsymbol{\nu}^t, \boldsymbol{\tau}^t, \boldsymbol{\mu}^t) = \pm 1$. Indeed the determinant is positive since for small t we have

$$\begin{aligned} \det(\boldsymbol{\nu}^t, \boldsymbol{\tau}^t, \boldsymbol{\mu}^t) &= \det\left(\frac{\partial \mathbf{T}_t^{-\top} \boldsymbol{\nu}}{\|\partial \mathbf{T}_t \boldsymbol{\tau}\|}, \frac{\partial \mathbf{T}_t \boldsymbol{\tau}}{\|\partial \mathbf{T}_t^{-\top} \boldsymbol{\nu}\|}, \left(\mathbf{I} - \frac{\partial \mathbf{T}_t^{-\top} \boldsymbol{\nu}}{\|\partial \mathbf{T}_t^{-\top} \boldsymbol{\nu}\|} \otimes \frac{\partial \mathbf{T}_t^{-\top} \boldsymbol{\nu}}{\|\partial \mathbf{T}_t^{-\top} \boldsymbol{\nu}\|}\right) \partial \mathbf{T}_t^{-\top} \boldsymbol{\mu}\right) \\ &= \det\left(\frac{\partial \mathbf{T}_t^{-\top} \boldsymbol{\nu}}{\|\partial \mathbf{T}_t \boldsymbol{\tau}\|}, \frac{\partial \mathbf{T}_t \boldsymbol{\tau}}{\|\partial \mathbf{T}_t^{-\top} \boldsymbol{\nu}\|}, \partial \mathbf{T}_t^{-\top} \boldsymbol{\mu}\right) = \det(\partial \mathbf{T}_t^{-\top}) \det\left(\frac{\boldsymbol{\nu}}{\|\partial \mathbf{T}_t \boldsymbol{\tau}\|}, \frac{\partial \mathbf{T}_t^\top \partial \mathbf{T}_t \boldsymbol{\tau}}{\|\partial \mathbf{T}_t^{-\top} \boldsymbol{\nu}\|}, \boldsymbol{\mu}\right) \\ &= \frac{\det(\partial \mathbf{T}_t^{-\top})}{\|\partial \mathbf{T}_t \boldsymbol{\tau}\| \|\partial \mathbf{T}_t^{-\top} \boldsymbol{\nu}\|} \underbrace{\boldsymbol{\mu} \times \boldsymbol{\nu}}_{=\boldsymbol{\tau}} \cdot (\partial \mathbf{T}_t^\top \partial \mathbf{T}_t \boldsymbol{\tau}) = \frac{\det(\partial \mathbf{T}_t^{-\top})}{\|\partial \mathbf{T}_t \boldsymbol{\tau}\| \|\partial \mathbf{T}_t^{-\top} \boldsymbol{\nu}\|} \|\partial \mathbf{T}_t \boldsymbol{\tau}\|^2 > 0. \end{aligned}$$

□

Thus, using Lemma 3.2 the perturbation of (3.15) reads by changing variables together with (3.22) and $\partial^S(\boldsymbol{\nu}_t \circ \mathbf{T}_t) = (\partial^{S_t} \boldsymbol{\nu}_t) \circ \mathbf{T}_t \mathbf{A}^{-\top}(t)$

$$\begin{aligned} \mathcal{L}^t(\mathcal{T}_h^t, \kappa_t, \sigma_t) &= \sum_{T \in \mathcal{T}_h} \left(\int_T w_t 2\kappa_b \left(\frac{1}{2} \kappa - H_0 \right)^2 + w_t (\kappa + \text{tr}(\partial^S \boldsymbol{\nu}^t \mathbf{A}^\top(t)) \sigma) ds \right. \\ &\quad \left. + \int_{\partial T} w_t^E \left(\frac{\pi}{2} - \angle(\boldsymbol{\mu}^t, \mathbf{P}_{\boldsymbol{\tau}^t}^\perp(\{\boldsymbol{\nu}\})) \right) \sigma d\gamma \right) + c_A J_{\text{surf}}(\mathcal{T}_h^t) + c_V J_{\text{vol}}(\mathcal{T}_h^t). \end{aligned} \quad (3.28)$$

4. SHAPE DERIVATIVES

In this section we derive all shape derivatives [12, 50] involved for the perturbed Lagrangian (3.28) using the notation from the previous section. For completeness we present all shape derivatives, but concentrate on the more involved shape operator and corresponding distributional jump term. Further, the state and adjoint state problems used in the solving algorithm in Section 5 are presented. As before we assume that $\mathcal{S} \subset \mathbf{R}^3$ is a smooth embedded sub-manifold of dimension two. We stress that the two-dimensional case with a one-dimensional sub-manifold directly follows.

4.1. Shape derivative of normal/tangential vectors and constraints. We start with the following well-known, but crucial, shape-derivatives of the geometric quantities.

Lemma 4.1. *Let w_t , w_t^E , $\boldsymbol{\tau}^t$, $\boldsymbol{\nu}^t$, and $\boldsymbol{\mu}^t$ defined as in (3.25), (3.26), and (3.27). Then for every $T \in \mathcal{T}_h$ and $E \in \mathcal{E}_h$:*

$$\frac{d}{dt} \boldsymbol{\nu}^t|_{t=0} = -\partial^S \mathbf{X}^\top \boldsymbol{\nu} \quad \text{in } [C(T)]^3, \quad (4.1a)$$

$$\frac{d}{dt} \boldsymbol{\tau}^t|_{t=0} = (\mathbf{I} - \boldsymbol{\tau} \otimes \boldsymbol{\tau}) \partial^S \mathbf{X} \boldsymbol{\tau} \quad \text{in } [C(E)]^3, \quad (4.1b)$$

$$\frac{d}{dt} \boldsymbol{\mu}^t|_{t=0} = ((\mathbf{I} - \boldsymbol{\tau} \otimes \boldsymbol{\tau}) \partial^S \mathbf{X} - \partial^S \mathbf{X}^\top) \boldsymbol{\mu} \quad \text{in } [C(E)]^3, \quad (4.1c)$$

$$\frac{d}{dt} w_t|_{t=0} = \text{div}^S(\mathbf{X}) \quad \text{in } C(T), \quad (4.1d)$$

$$\frac{d}{dt} w_t^E|_{t=0} = \partial^S \mathbf{X}_{\boldsymbol{\tau} \boldsymbol{\tau}} := \partial^S \mathbf{X} \boldsymbol{\tau} \cdot \boldsymbol{\tau} \quad \text{in } C(E), \quad (4.1e)$$

where convergence in $C(T)$ has to be understood with respect to the norm $\|f\|_{C(\mathcal{T}_h)} := \max_{x \in \mathcal{T}_h} \|f(x)\|$, and analogously for $C(E)$.

Proof. Recalling $\frac{d}{dt}\partial\mathbf{T}_t^{-\top}|_{t=0} = -\partial\mathbf{X}^\top$ and the formula (3.26) for $\boldsymbol{\nu}^t$, we compute using the product rule:

$$\frac{d}{dt}(\boldsymbol{\nu}^t)|_{t=0} = \frac{d}{dt} \frac{\partial\mathbf{T}_t^{-\top}\boldsymbol{\nu}}{\|\partial\mathbf{T}_t^{-\top}\boldsymbol{\nu}\|}|_{t=0} = -\partial\mathbf{X}^\top\boldsymbol{\nu} + (\partial\mathbf{X}\boldsymbol{\nu} \cdot \boldsymbol{\nu})\boldsymbol{\nu} = -(\mathbf{I} - \boldsymbol{\nu} \otimes \boldsymbol{\nu})\partial\mathbf{X}^\top\boldsymbol{\nu} = -\partial^S\mathbf{X}^\top\boldsymbol{\nu}.$$

The other identities follow analogously together with $\frac{d}{dt}\det(\partial\mathbf{T}_t)|_{t=0} = \operatorname{div}^S(\mathbf{X})$. \square

As an immediate consequence we obtain for the constraints:

Lemma 4.2. *The shape derivatives of the surface and volume constraint in direction $\mathbf{X} \in C_c^1(\mathbf{R}^d)^d$ are given by*

$$DJ_{\text{surf}}(\mathcal{T}_h)(\mathbf{X}) = 2(|\mathcal{T}_h| - A_0) \int_{\mathcal{T}_h} \operatorname{div}^S(\mathbf{X}) \, ds, \quad (4.2)$$

$$DJ_{\text{vol}}(\mathcal{T}_h)(\mathbf{X}) = 2(|\Omega_h| - V_0) \int_{\mathcal{T}_h} \mathbf{X} \cdot \boldsymbol{\nu} \, ds. \quad (4.3)$$

Proof. The shape derivatives of J_{surf} and J_{vol} are standard and therefore omitted. \square

4.2. Shape derivative of shape operator.

Lemma 4.3. *There holds for $\mathbf{u} \in C^1(\mathbf{R}^3)^3$ and $\mathbf{u}_t := \mathbf{u} \circ \mathbf{T}_t^{-1}$*

$$\frac{d}{dt}(\partial^{S_t}\mathbf{u}_t) \circ \mathbf{T}_t|_{t=0} = \partial^S\mathbf{u} (2\operatorname{Sym}(\boldsymbol{\nu} \otimes \boldsymbol{\nu}\partial^S\mathbf{X}) - \partial^S\mathbf{X}). \quad (4.4)$$

Proof. We have for $t \geq 0$ by the chain rule

$$(\partial^{S_t}\mathbf{u}_t) \circ \mathbf{T}_t = \partial^S\mathbf{u} \mathbf{A}(t)^\top \quad (4.5)$$

with $\mathbf{A}(t)$ as in (3.22). Moreover, with (3.24) it follows by differentiating (4.5) that

$$\frac{d}{dt}(\partial^{S_t}\mathbf{u}_t) \circ \mathbf{T}_t|_{t=0} = \partial^S\mathbf{u} (\mathbf{A}^\top)'(0) = \partial^S\mathbf{u} (2\operatorname{Sym}(\boldsymbol{\nu} \otimes \boldsymbol{\nu}\partial^S\mathbf{X}) - \partial^S\mathbf{X}),$$

which finishes the proof. \square

Lemma 4.4. *For the shape operator $\partial^S\boldsymbol{\nu}$ and its trace there hold*

$$\frac{d}{dt}(\partial^{S_t}\boldsymbol{\nu}_t) \circ \mathbf{T}_t|_{t=0} = \partial^S\boldsymbol{\nu} (2\operatorname{Sym}(\boldsymbol{\nu} \otimes \boldsymbol{\nu}\partial^S\mathbf{X}) - \partial^S\mathbf{X}) - \operatorname{hess}(\mathbf{X})(\boldsymbol{\nu}) - \partial^S\mathbf{X}^\top\partial^S\boldsymbol{\nu}, \quad (4.6)$$

$$\frac{d}{dt}\operatorname{tr}(\partial^{S_t}\boldsymbol{\nu}_t) \circ \mathbf{T}_t|_{t=0} = -\Delta^S\mathbf{X} \cdot \boldsymbol{\nu} - 2\partial^S\mathbf{X} : \partial^S\boldsymbol{\nu}, \quad (4.7)$$

where $\operatorname{hess}(\mathbf{X})$ denotes the surface Hessian of \mathbf{X} and $\Delta^S\mathbf{X} := \operatorname{div}^S(\partial^S\mathbf{X})$ the Laplace-Beltrami operator.

Further, with a continuous and piece-wise smooth function σ there holds for the weak form

$$\int_T -(\Delta^S\mathbf{X} \cdot \boldsymbol{\nu} + 2\partial^S\mathbf{X} : \partial^S\boldsymbol{\nu})\sigma \, ds = \int_T \partial^S\mathbf{X}\partial^S\sigma \cdot \boldsymbol{\nu} - \partial^S\mathbf{X} : \partial^S\boldsymbol{\nu}\sigma \, ds - \int_{\partial T} \partial^S\mathbf{X}\boldsymbol{\mu} \cdot \boldsymbol{\nu} \sigma \, d\gamma. \quad (4.8)$$

Proof. With the product rule and Lemma 4.3 there holds

$$\frac{d}{dt}(\partial^{S_t}\boldsymbol{\nu}_t) \circ \mathbf{T}_t|_{t=0} = \partial^S \left(\frac{d}{dt}(\boldsymbol{\nu}_t) \circ \mathbf{T}_t|_{t=0} \right) + \partial^S\boldsymbol{\nu} (2\operatorname{Sym}(\boldsymbol{\nu} \otimes \boldsymbol{\nu}\partial^S\mathbf{X}) - \partial^S\mathbf{X})$$

and further with (4.1a)

$$\partial^S \left(\frac{d}{dt}(\boldsymbol{\nu}_t) \circ \mathbf{T}_t|_{t=0} \right) = -\partial^S (\partial^S\mathbf{X}^\top\boldsymbol{\nu}) = -\partial^S\mathbf{X}^\top\partial^S\boldsymbol{\nu} - \operatorname{hess}(\mathbf{X})(\boldsymbol{\nu}).$$

For the trace of the shape operator we compute

$$\begin{aligned} & \text{tr}(\partial^S \boldsymbol{\nu} (2 \text{Sym}(\boldsymbol{\nu} \otimes \boldsymbol{\nu} \partial^S \mathbf{X}) - \partial^S \mathbf{X}) - \text{hess}(\mathbf{X})(\boldsymbol{\nu}) - \partial^S \mathbf{X}^\top \partial^S \boldsymbol{\nu}) = \\ & 2 \partial^S \boldsymbol{\nu} : (\text{Sym}(\boldsymbol{\nu} \otimes \boldsymbol{\nu} \partial^S \mathbf{X})) - \partial^S \boldsymbol{\nu} : \partial^S \mathbf{X} - \text{tr}(\text{hess}(\mathbf{X})(\boldsymbol{\nu})) - \partial^S \mathbf{X} : \partial^S \boldsymbol{\nu} = \\ & 2 \underbrace{\partial^S \boldsymbol{\nu} : (\boldsymbol{\nu} \otimes \boldsymbol{\nu} \partial^S \mathbf{X})}_{=0} - \text{tr}(\text{hess}(\mathbf{X})(\boldsymbol{\nu})) - 2 \partial^S \mathbf{X} : \partial^S \boldsymbol{\nu} = -\Delta^S \mathbf{X} \cdot \boldsymbol{\nu} - 2 \partial^S \mathbf{X} : \partial^S \boldsymbol{\nu}, \end{aligned}$$

where we used that $\partial^S \boldsymbol{\nu}^\top \boldsymbol{\nu} = 0$. The weak form (4.8) follows directly with integration by parts. \square

We will also need the shape derivative of the distributional part of the curvature:

Lemma 4.5. *There holds*

$$\frac{d}{dt} \angle(\boldsymbol{\mu}^t, \mathbf{P}_{\boldsymbol{\tau}^t}^\perp(\{\boldsymbol{\nu}\}))|_{t=0} = -\frac{(\partial^S \mathbf{X} - \partial^S \mathbf{X}^\top) \boldsymbol{\mu} \cdot \{\boldsymbol{\nu}\}}{\sqrt{1 - (\boldsymbol{\mu} \cdot \{\boldsymbol{\nu}\})^2}}. \quad (4.9)$$

Proof. See Appendix A. \square

We emphasize that the same result holds if we would neglect the projection $\mathbf{P}_{\boldsymbol{\tau}^t}^\perp(\cdot)$ and solely consider the term $\angle(\boldsymbol{\mu}^t, \{\boldsymbol{\nu}\})$. However, for the second shape derivatives, which is important when considering a shape Newton algorithm, the results would differ.

4.3. Shape derivative, state, and adjoint state problem. The parameterized Lagrangian is defined by

$$G(t, \kappa, \sigma) := \mathcal{L}^t(\mathcal{T}_h^t, \kappa \circ \mathbf{T}_t^{-1}, \sigma \circ \mathbf{T}_t^{-1}). \quad (4.10)$$

Therefore the shape derivative can be computed by (see [32])

$$D\mathcal{J}(\mathcal{T}_h)(\mathbf{X}) = \partial_t G(0, \kappa, \sigma), \quad (4.11)$$

where (κ, σ) solve

$$\begin{aligned} & \text{find } \kappa, \text{ such that } \partial_\sigma G(0, \kappa, \sigma)(\delta\sigma) = 0 \quad \text{for all } \delta\sigma \in V_h(\mathcal{T}_h), \\ & \text{find } \sigma, \text{ such that } \partial_\kappa G(0, \kappa, \sigma)(\delta\kappa) = 0 \quad \text{for all } \delta\kappa \in V_h(\mathcal{T}_h), \end{aligned} \quad (4.12)$$

with

$$\partial_\kappa G(0, \kappa, \sigma)(\delta\kappa) = \int_S 2\kappa_b \left(\frac{1}{2} \kappa - H_0 \right) \delta\kappa + \delta\kappa \sigma \, ds, \quad (4.13)$$

$$\partial_\sigma G(0, \kappa, \sigma)(\delta\sigma) = \sum_{T \in \mathcal{T}_h} \left(\int_T \kappa \delta\sigma + \text{tr}(\partial^S \boldsymbol{\nu}) \delta\sigma \, ds + \int_{\partial T} \left(\frac{\pi}{2} - \angle(\boldsymbol{\mu}, \mathbf{P}_{\boldsymbol{\tau}}^\perp(\{\boldsymbol{\nu}\})) \right) \delta\sigma \, d\gamma \right). \quad (4.14)$$

Adding up all terms together with Lemma 4.2 the shape derivative of Lagrangian (3.15) reads

$$\begin{aligned} D\mathcal{J}(\mathcal{T}_h)(\mathbf{X}) = & \sum_{T \in \mathcal{T}_h} \left(\int_T \text{div}^S(\mathbf{X}) 2\kappa_b \left(\frac{1}{2} \kappa - H_0 \right)^2 + \text{div}^S(\mathbf{X}) \sigma \kappa + \text{div}^S(\mathbf{X}) \text{tr}(\partial^S \boldsymbol{\nu}) \sigma \right. \\ & + \partial^S \mathbf{X} \partial^S \sigma \cdot \boldsymbol{\nu} - \partial^S \mathbf{X} : \partial^S \boldsymbol{\nu} \sigma \, ds - \int_{\partial T} \partial^S \mathbf{X} \boldsymbol{\mu} \cdot \boldsymbol{\nu} \sigma \, d\gamma \\ & + 2c_A(|\mathcal{T}_h| - A_0) \int_T \text{div}^S(\mathbf{X}) \, ds + 2c_V(|\Omega_h| - V_0) \int_T \mathbf{X} \cdot \boldsymbol{\nu} \, ds \\ & \left. + \int_{\partial T} (\partial^S \mathbf{X}_{\boldsymbol{\tau}\boldsymbol{\tau}} \left(\frac{\pi}{2} - \angle(\boldsymbol{\mu}, \{\boldsymbol{\nu}\}) \right) + \frac{(\partial^S \mathbf{X} - \partial^S \mathbf{X}^\top) \boldsymbol{\mu} \cdot \{\boldsymbol{\nu}\}}{\sqrt{1 - (\boldsymbol{\mu} \cdot \{\boldsymbol{\nu}\})^2}}) \sigma \, d\gamma \right). \end{aligned} \quad (4.15)$$

In the lowest order case, $\mathcal{T}_{h,1}$, there holds $\mathbf{X} \in [V_h^1(\mathcal{T}_h)]^3$ and $\boldsymbol{\nu}|_T = \text{const}$, and therefore (4.15) simplifies to

$$\begin{aligned} D\mathcal{J}(\mathcal{T}_h)(\mathbf{X}) = & \sum_{T \in \mathcal{T}_h} \left(\int_T \text{div}^S(\mathbf{X}) 2\kappa_b \left(\frac{1}{2}\kappa - H_0 \right)^2 + \text{div}^S(\mathbf{X}) \sigma \kappa ds \right. \\ & + 2c_A(|\mathcal{T}_h| - A_0) \int_T \text{div}^S(\mathbf{X}) ds + 2c_V(|\Omega_h| - V_0) \int_T \mathbf{X} \cdot \boldsymbol{\nu} ds \\ & \left. + \int_{\partial T} (\partial^S \mathbf{X}_{\tau\tau} \left(\frac{\pi}{2} - \angle(\boldsymbol{\mu}, \{\boldsymbol{\nu}\}) \right) + \frac{(\partial^S \mathbf{X} - \partial^S \mathbf{X}^\top) \boldsymbol{\mu} \cdot \{\boldsymbol{\nu}\}}{\sqrt{1 - (\boldsymbol{\mu} \cdot \{\boldsymbol{\nu}\})^2}}) \sigma d\gamma \right). \end{aligned} \quad (4.16)$$

We observe that the lifting of the distributional shape operator $-\partial^S \boldsymbol{\nu}$ is done only by the boundary jump terms. For a one-dimensional sub-manifold in 2D the jump term in (4.15) simplifies as no deformation determinant is involved:

$$\begin{aligned} D\mathcal{J}^{2D}(\mathcal{T}_h)(\mathbf{X}) = & \sum_{T \in \mathcal{T}_h} \left(\int_T \text{div}^S(\mathbf{X}) 2\kappa_b (\kappa - H_0)^2 + \text{div}^S(\mathbf{X}) \sigma \kappa + \text{div}^S(\mathbf{X}) \text{tr}(\partial^S \boldsymbol{\nu}) \sigma \right. \\ & + \partial^S \mathbf{X} \partial^S \sigma \cdot \boldsymbol{\nu} - \partial^S \mathbf{X} : \partial^S \boldsymbol{\nu} \sigma ds - \int_{\partial T} \partial^S \mathbf{X} \boldsymbol{\mu} \cdot \boldsymbol{\nu} \sigma d\gamma \\ & + 2c_A(|\mathcal{T}_h| - A_0) \int_T \text{div}^S(\mathbf{X}) ds + 2c_V(|\Omega_h| - V_0) \int_T \mathbf{X} \cdot \boldsymbol{\nu} ds \\ & \left. + \int_{\partial T} \frac{(\partial^S \mathbf{X} - \partial^S \mathbf{X}^\top) \boldsymbol{\mu} \cdot \{\boldsymbol{\nu}\}}{\sqrt{1 - (\boldsymbol{\mu} \cdot \{\boldsymbol{\nu}\})^2}} \sigma d\gamma \right). \end{aligned} \quad (4.17)$$

4.4. Stabilization of element-areas. With the penalty term $c_A(|\mathcal{T}_h| - A_0)^2$ we control the total surface area to be close to a prescribed value A_0 . As the solution is invariant under re-parameterization it may happen, however, that some elements shrink or increase their local area, leading to a deterioration of the shape regularity of the elements. To mitigate this possible mesh-degeneration we use a local area preservation constraint (see [3]):

$$\sum_{T \in \mathcal{T}_h} c_{A_{\text{loc}}, T} (|T| - |T_0|)^2, \quad (4.18)$$

where T_0 denotes the element area on the initial shape. Further, its shape-derivative is of the same form as the global area constraint.

Other approaches to prevent ill-shaped meshes are regularity techniques as viscous regularization [34] or remeshing, including local refinement, coarsening, and smoothing [41, 7]. Note that for free-boundary problems the question of the placement of additionally inserted nodes to obtain a consistent mesh is not straight-forward, especially for high-order curved shapes.

5. SOLVING ALGORITHM

5.1. Basic algorithm. Let \mathcal{T}_h be a fixed initial surface and let $\mathbf{H} = H^1(\mathcal{T}_h)^3$ be equipped with the scalar product

$$(\mathbf{V}, \mathbf{W})_{\mathbf{H}} := \int_{\mathcal{T}_h} \partial^S \mathbf{V} : \partial^S \mathbf{W} + \varepsilon \mathbf{V} \cdot \mathbf{W} ds, \quad \varepsilon > 0. \quad (5.1)$$

Here, $\varepsilon > 0$ is needed to guarantee positive definiteness, as we will consider closed surfaces without a possible boundary, which will be fixed to $\varepsilon := 1 \times 10^{-10}$ throughout this work. We emphasize that the full gradient ∂^S leads to more regular displacement updates than considering only its symmetric part $\partial^S \mathbf{V} + \partial^S \mathbf{V}^\top$. Further, the constant ε in (5.1) should

be chosen to be small as otherwise the mass matrix gains more weight also leading to worse mesh-quality updates. Then, the gradient $\nabla^H g(\mathbf{V})$ is defined by

$$\partial g(\mathbf{V})(\mathbf{W}) = (\nabla^H g(\mathbf{V}), \mathbf{W})_H \quad \forall \mathbf{W} \in H, \quad (5.2)$$

where the mapping g is defined by

$$\mathbf{V} \mapsto g(\mathbf{V}) := \mathcal{J}((\text{Id} + \mathbf{V})(\mathcal{T}_h)) \quad (5.3)$$

and there holds for the derivative of g at \mathbf{V} in direction \mathbf{W} (see [23, 27])

$$\partial g(\mathbf{V})(\mathbf{W}) = D\mathcal{J}((\text{Id} + \mathbf{V})(\mathcal{T}_h))(\mathbf{W} \circ (\text{Id} + \mathbf{V})^{-1}). \quad (5.4)$$

The shape optimization algorithm reads as follows:

Algorithm 1 gradient algorithm

```

1: Input: surface  $\mathcal{T}_h^0$ ,  $n = 0$ ,  $N_{\max} > 0$ ,  $\epsilon > 0$ ,  $\alpha > 0$ 
2: Output: optimal shape  $\mathcal{T}_h^*$ 
3: while  $n \leq N_{\max}$  and  $|\nabla \mathcal{J}(\mathcal{T}_h^n)| > \epsilon$  do
4:   if  $\mathcal{J}((\text{Id} - \alpha \nabla \mathcal{J}(\mathcal{T}_h^n))(\mathcal{T}_h^n)) \leq \mathcal{J}(\mathcal{T}_h^n)$  then
5:      $\mathcal{T}_h^{n+1} \leftarrow (\text{Id} - \alpha \nabla \mathcal{J}(\mathcal{T}_h^n))(\mathcal{T}_h^n)$ 
6:      $n \leftarrow n + 1$ 
7:     increase  $\alpha$ 
8:   else
9:     reduce  $\alpha$ 
10:  end if
11: end while
    
```

The input quantities are the initial shape \mathcal{T}_h^0 , the maximal number of optimization steps $N_{\max} > 0$, a threshold ϵ for the shape gradient residuum, and the initial step-size α . A line-search is performed by testing if the goal functional, the mean curvature together with the volume and area constraints, is decreasing. Otherwise the step-size α will be reduced. If the step gets accepted it is possible to increase α to gain a faster convergence towards the minimum. Note, however, that a raise of α has to be done carefully as the shape may run e.g. into singularities.

One iteration step of Algorithm 5.1 involves:

- (1) For a fixed surface \mathcal{T}_h^n average the corresponding normal vector $\boldsymbol{\nu}$ and solve for κ , σ the state and adjoint state equation (4.12).
- (2) With the new κ and σ calculate the gradient by computing the shape derivative (4.15).

To reduce the possibility to get stuck in a local minimum a non-monotone gradient method is considered, where the next gradient step needs to result in a lower cost then the maximum of the last $M = 5$ energies to be accepted. Therefore the right-hand side of Line 4 in Algorithm 5.1 changes to $\leq \max_{i=0}^{M-1} \mathcal{J}(\mathcal{T}_h^{n-i})$.

After convergence the parameters involving the area and volume constraints can be increased and the algorithm is repeated.

For simplicity we keep with the standard (non-monotone) gradient algorithm. Other methods as l-BFGS or nonlinear conjugate gradient algorithms (NCG) to speed up the convergence and relying on the first shape derivative can directly be adapted; see, e.g., [5, 46, 27].

5.2. Improved surface preservation. In the shape optimization algorithm three different parameters regulating the volume and area constraints are involved: c_V , c_A , and $c_{A_{\text{loc},T}}$. It is desirable having as less parameters as possible while preserving the convergence and performance of the algorithm. In the case where the initial shape already has the appropriate area it is possible to generate deformation updates such that the area gets close to being constant.

For this purpose, instead of computing the shape gradient in H^1 via inner product (5.2) we incorporate a divergence free condition by solving a Stokes problem, where an additional pressure-like unknown p is introduced to enforce that the displacement increment is divergence-free, i.e., the surface area should be linearly preserved. Given a vector field \mathbf{V} , we seek $(\mathbf{X}, p) \in \mathbf{H} \times H^1(\mathcal{T}_h)$, such that

$$(\mathbf{X}, \mathbf{W})_{\mathbf{H}} + (p, \operatorname{div}(\mathbf{W}))_{L^2} = \partial g(\mathbf{V})(\mathbf{W}), \quad \text{for all } \mathbf{W} \in \mathbf{H}, \quad (5.5a)$$

$$(q, \operatorname{div}(\mathbf{X}))_{L^2} = 0, \quad \text{for all } q \in H^1(\mathcal{T}_h). \quad (5.5b)$$

The function \mathbf{X} is the shape gradient $\nabla^{\mathbf{H}} g(\mathbf{V})$ with respect to \mathbf{H} with the additional condition that $\operatorname{div}(\mathbf{X}) = 0$ in a weak sense. Note, that this requires a Stokes stable finite element pairing for \mathbf{X} and p . The famous Taylor-Hood pairing for example requires that p is of one polynomial order lower than \mathbf{X} and thus, quadratic polynomials for the deformation fields have to be used in combination with a linear approximation of the pressure. Other choices, such as the MINI element, or a pressure-projection stabilized equal order pair [16] are possible.

Using this procedure any moderately choice of $c_A > 0$ leads to shapes with stable surface area (we observed that the error evolves with less then 1%). Setting $c_A = 0$ is invalid as in this case we loose control over the global area constraint, having only linear divergence-free updates. As a result only the volume constraint has to be adapted after the shape optimization algorithm determinates.

The obvious disadvantage of (5.5) is the increased computational effort, since now a saddle-point problem has to be solved in each step instead of a positive definite one.

5.3. Automatic shape derivatives in NGSolve. In Section 4 all shape derivatives were computed analytically such that the shape optimization Algorithm 5.1 can directly be applied if the current (deformed) meshes are accessible. One possibility consists of (manually) deforming all vertices of the mesh during each optimization step and then computing the state and adjoint state problems as well as the next shape derivative on it. This, however, is not applicable for curved elements. Instead we use an ALE (arbitrary Lagrangian Eulerian) technique, where a mesh (mostly the initial shape) is fixed and all computations are performed on it. Therefore, the involved deformation gradients and determinants have to be incorporated, which is straight forward but error prone and can lead to complicated or confusing expressions. In this work we use the open source finite element software NGSolve¹ [45], where the method `SetDeformation` can be used to avoid the manual computation of the transformations and chain rules. In the supplementary material file a full code example including a detailed description can be found.

To demonstrate how the deformation of a mesh is realized we consider the following lines of code:

```
1 mesh.SetDeformation(displacement)
2 A.Assemble()
3 mesh.UnsetDeformation()
```

¹www.ngsolve.org

where A corresponds to the standard stiffness bilinear form

$$a : H^1(\Omega) \times H^1(\Omega) \rightarrow \mathbf{R}, \quad a(u, v) = \int_{\Omega} \nabla u \cdot \nabla v \, dx,$$

`mesh` is the initial shape \mathcal{T}_h^0 , and the object `displacement` knows how the mesh has to be deformed leading to the current shape \mathcal{T}_h^n . Then, everything between `SetDeformation` and `UnsetDeformation` gets assembled as it was on the current configuration by using the appropriate transformation rules, namely

$$a(u, v) = \int_{\Omega} J \mathbf{F}^{\top} \nabla u \cdot \mathbf{F}^{\top} \nabla v \, dx$$

with $\mathbf{F} = \mathbf{I} + \nabla \text{displacement}$ and $J = \det(\mathbf{F})$.

The computation of shape derivatives can be challenging and also error prone due complicated expressions. In the recent publication [23] the fully automated and semi-automated computation of shape derivatives in NGSolve was presented. For instance, to compute the shape derivative (4.15), excluding the area and volume constraint, one can consider for fixed κ and σ the linear form (compare (3.28))

$$F(\kappa, \sigma) = \sum_{T \in \mathcal{T}_h} \left(\int_T 2\kappa_b \left(\frac{1}{2}\kappa - H_0 \right)^2 + (\kappa + \text{tr}(\partial^{\mathcal{S}} \boldsymbol{\nu})) \sigma \, ds + \int_{\partial T} \left(\frac{\pi}{2} - \angle(\boldsymbol{\mu}, \mathbf{P}_{\boldsymbol{\tau}}^{\perp}(\{\boldsymbol{\nu}\})) \right) \sigma \, d\gamma \right)$$

which can be written symbolically in Python as

```
1 def F(kappa, sigma):
2     return (2*kappa*(1/2*kappa-H0)**2 + (kappa + Trace(Grad(nsurf)))*sigma)*ds + (pi
    /2-acos(nel*nav))*sigma*ds(element_boundary=True)
```

where `nav` := $\mathbf{P}_{\boldsymbol{\tau}}^{\perp}(\{\boldsymbol{\nu}\})$, and then call the function `DiffShape` to obtain $DF(\mathcal{T}_h, \kappa, \sigma)(\mathbf{X})$. We emphasise that in the final code we neglected the nonlinear projection operator $\mathbf{P}_{\boldsymbol{\tau}}^{\perp}(\cdot)$ saving unnecessary computations as noted below Lemma 4.5.

```
1 fesH = VectorH1(mesh, order=order)
2 X = fesH.TestFunction()
3
4 f = LinearForm(fesH)
5 f += F(kappa, sigma).DiffShape(X)
6 f.Assemble()
```

This procedure can directly be combined with the `SetDeformation` method from before to compute the shape derivative automatically on the current configuration without actually changing the mesh.

Due to the integral form of the constraints the utilized form for the shape derivative is given by e.g.,

$$\frac{d}{dt} c_V (|\mathbf{T}_t(\Omega_h)| - |V_0|)^2|_{t=0} = 2 c_V (|\Omega_h| - |V_0|) \frac{d}{dt} |\mathbf{T}_t(\Omega_h)||_{t=0}$$

and then the `DiffShape` function can be applied to $|\Omega_h| = \int_{\mathcal{T}_h} \frac{1}{d} \mathbf{x} \cdot \boldsymbol{\nu} \, ds$ to compute the full shape derivative.

This tool of automatic shape derivatives can also be extremely helpful in terms of cross-checking the manually computed shape derivatives or an efficient and utilised for fast testing of changes of the equations without the necessity of recomputing all derivatives by hand.

6. NUMERICAL EXAMPLES

In this section, we demonstrate the performance of the proposed method. First, we test the mean curvature computation of our method showing the pertinence of the non-standard boundary jump term measuring the angle between two neighbored triangles. Particularly in the lowest order case when approximating the curvature with linear polynomials on an affine triangulation the inner part of (3.14) vanishes as the normal vector is piece-wise constant in this case (compare Figure 3.1). Then, we present two benchmark examples for equilibrium shapes motivated by cell membranes including non-zero spontaneous curvature.

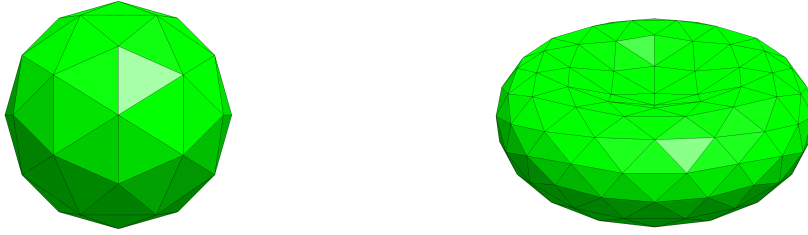


FIGURE 6.1. Icosahedron and biconcave-oblate.

6.1. Prescribed configurations of sphere and biconcave-oblate. We compute the Canham–Helfrich–Evans energy (1.1) as in [3] with $\kappa_b = 1$ of a given sphere of radius $R = 1$ and a biconcave-oblate described by the embedding

$$x = \sin(u) \sin(v), \quad y = \sin(u) \cos(v), \quad z = F(\cos(u)),$$

where $(u, v) \in [-\pi/2, \pi/2] \times [0, 2\pi]$ are the parametric coordinates of a sphere and $F(p) = 0.54353p + 0.121435p^3 - 0.561365p^5$.

The sphere is approximated by an icosahedron and a regular subdivision by dividing each triangle into four sub-triangles. For the biconcave-oblate the points of the icosahedron are appropriately transformed with $F(\cdot)$, compare Figure 6.1. The results for the lowest order method can be found in Figure 6.2 and 6.3 on the left, which converge to the correct values.

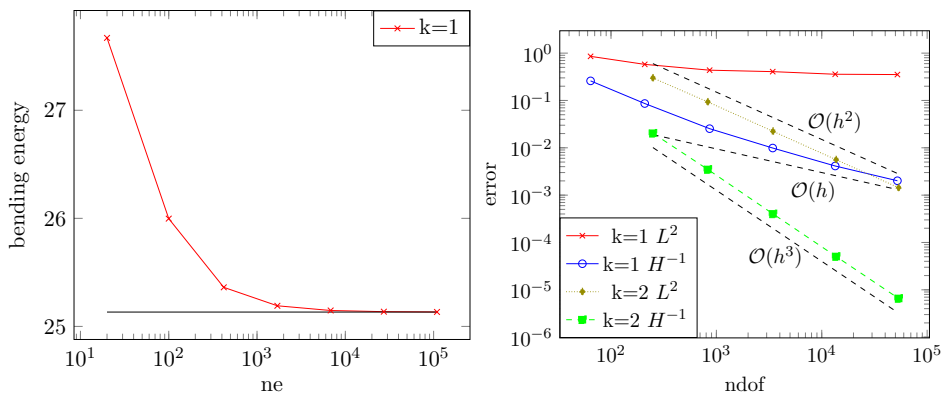


FIGURE 6.2. Left: Bending energy of icosahedron with lowest-order elements with respect to number of elements (ne). Exact value: 8π . Right: L^2 and H^{-1} error for unstructured meshes with linear and quadratic elements with respect to the number of degrees of freedom (ndof).

Next, we consider a sequence of non-nested unstructured meshes generated by NETGEN [44] approximating the sphere and biconcave-oblate with linear and quadratic polynomials

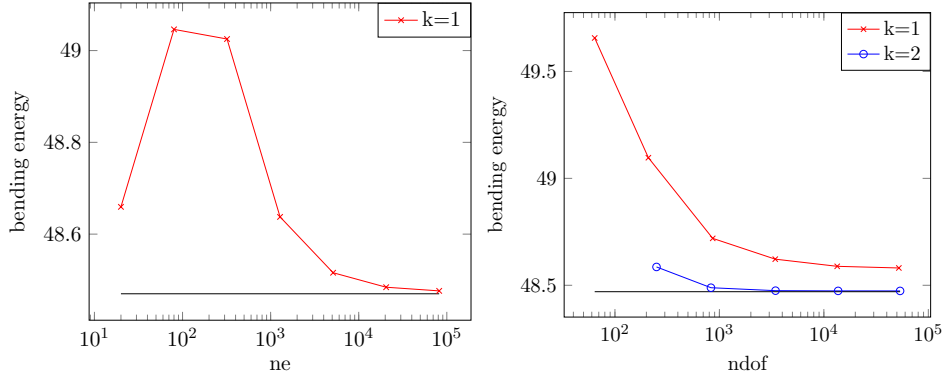


FIGURE 6.3. Left: Bending energy of icosahedron with lowest-order elements with respect to number of elements. Right: L^2 -norm of bending energy for unstructured meshes with linear and quadratic elements with respect to number of degrees of freedom. Reference value is 48.47.

for our method. In the second case the geometry is isoparametrically curved. As depicted in Figure 6.2 and 6.3 on the right the high-order method converges to the exact and reference value, respectively, in the L^2 - and H^{-1} -norm, namely

$$\|\kappa_h - \kappa_{\text{ref}}\|_{L^2}^2 := \int_S |\kappa_h - \kappa_{\text{ref}}|^2 ds, \quad \|\kappa_h - \kappa_{\text{ref}}\|_{H^{-1}} := \sup_{\sigma \in H^1(\mathcal{S})} \frac{\langle \kappa_h - \kappa_{\text{ref}}, \sigma \rangle}{\|\sigma\|_{H^1}}.$$

As observed in Figure 6.2 only the convergence rates differ, namely quadratic and cubic order, respectively. Note, that for the H^{-1} -norm we solve the auxiliary problem $-\Delta^S u_h = \kappa_h - \kappa_{\text{ref}}$ on \mathcal{T}_h with $u_h \in V_h^l(\mathcal{T}_h)$, $l > k$ as there holds $\|u\|_{H^1} = \|\kappa_h - \kappa_{\text{ref}}\|_{H^{-1}}$ in the continuous case. In the lowest order case, however, the L^2 -norm is not converging to the reference values, whereas the H^{-1} error does. This is in agreement with the fact that the (discrete) mean curvature is a distribution, rather than a function, and thus, in general, we cannot expect convergence for linear elements in the L^2 -norm.

The non-convergence of the lowest order curvature computation seems to be in contrast with the approach of using this curvature approximation for the shape optimization algorithm. Therefore, we consider the following test case: The same unstructured sequence of meshes approximating the sphere as used for the results in Figure 6.2 is taken and the shape optimization Algorithm 5.1 with A_0 , V_0 as the initial shape, and $\kappa_b = 0.01$, $c_V = 10/|V_0|$, $c_A = 5/|A_0|$, $c_{A_{\text{loc},T}} = 5/|T_0|$, and $N_{\text{max}} = 1000$ is used such that the initial shape is very close to a smooth sphere being the unique solution for this problem. In Figure 6.4 we can see that the shape optimization algorithm deforms the meshes only marginally in such a way that the L^2 -norm of the curvature error now converges, even with a quadratic rate. An explanation of this phenomenon is that on the one hand the curvature approximation enters the shape optimization step by being paired with an H^1 -test function, compare the $\kappa \sigma$ term in (4.15), enabling the convergent H^{-1} property and on the other hand the algorithm tries to minimize the (local) L^2 -norm of the mean curvature generating a sequence of optimal meshes - a quadratic convergence rate is optimal with respect to linear polynomials.

This supports and verifies the usage of linear approximations for the curvature as the shape optimization algorithm generates as a side-product meshes with beneficial curvature computation property.

6.2. Equilibrium shapes. In this example closed membranes with area 4π are subjected to different volume constraints leading to varying equilibrium shapes. We fix in this section

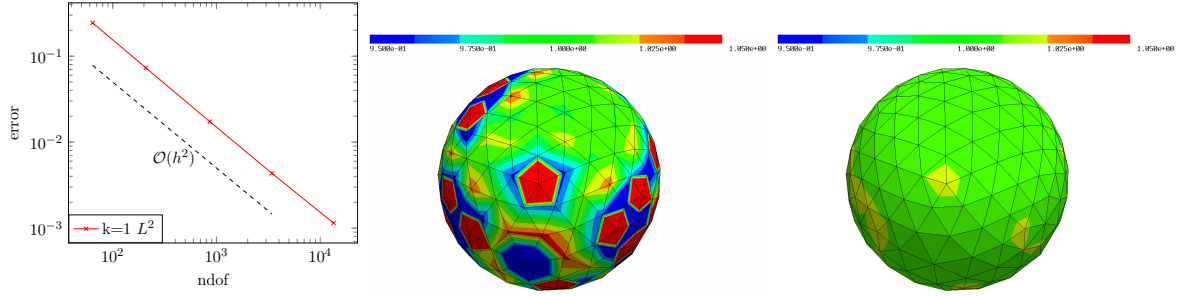


FIGURE 6.4. Left: L^2 -error of mean curvature at unstructured meshes with linear elements measured after 1000 shape-optimization steps with respect to number of degrees of freedom. Right: Mean curvature on initial shape and after 1000 optimization steps.

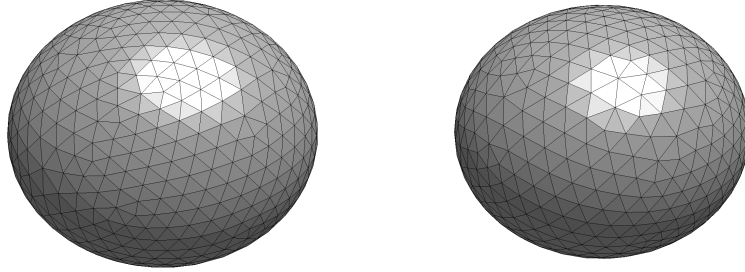


FIGURE 6.5. Initial unstructured prolate (left) and oblate (right) shapes with 1322 and 1258 triangles, respectively.

the parameters $\kappa_b = 0.01$, $H_0 = 0$, $c_V = \frac{1}{|V_0|}$, $c_A = \frac{2}{|A_0|}$, and $c_{A_{loc,T}} = \frac{1}{|T_0|}$ following [3]. As we have zero spontaneous curvature, $H_0 = 0$, the equilibrium shapes are axisymmetric and reference computations which can be calculated analytically by solving a 2D Euler-Lagrange ODE as in [14, 47]. To reproduce the phase diagram from [47] we use prolate ($c=1.1017$, $a=0.95$) and oblate ($c=0.9$, $a=1.5065$) initial shapes, see Figure 6.5, covering the prolate and oblate branches. When starting from a sphere it would be crucial to add a random noise on the initial shape to enable the shape optimization algorithm to deform the shape. As we consider unstructured grids for the oblate and prolate initial shape non-axisymmetric deformations are induced without additionally introducing noise. Otherwise it may happen that the initial shape gets directly stuck in a local minimum. In the phase diagram the normalized Canham–Helfrich–Evans energy (1.1) with respect to the bending energy of a perfect sphere

$$E^* = E/(8\pi\kappa_b) \quad (6.1)$$

is plotted against the so-called reduced volume

$$v := V / \left(\frac{4\pi}{3} \sqrt{\frac{A}{4\pi}}^3 \right). \quad (6.2)$$

Stable branches are given by prolate for $0.652 < v < 1$, oblate between $0.592 < v < 0.651$, and stomatocytes otherwise $0 < v < 0.591$ [47].

For the first test we consider the lowest order method (4.16) on the initial shapes from Figure 6.5 and then apply the shape optimization Algorithm 5.1 with the conservative choice of $\alpha = 0.025$, $N_{\max} = 100000$, $\epsilon = 1 \times 10^{-7}$ without increasing α after an accepted step.

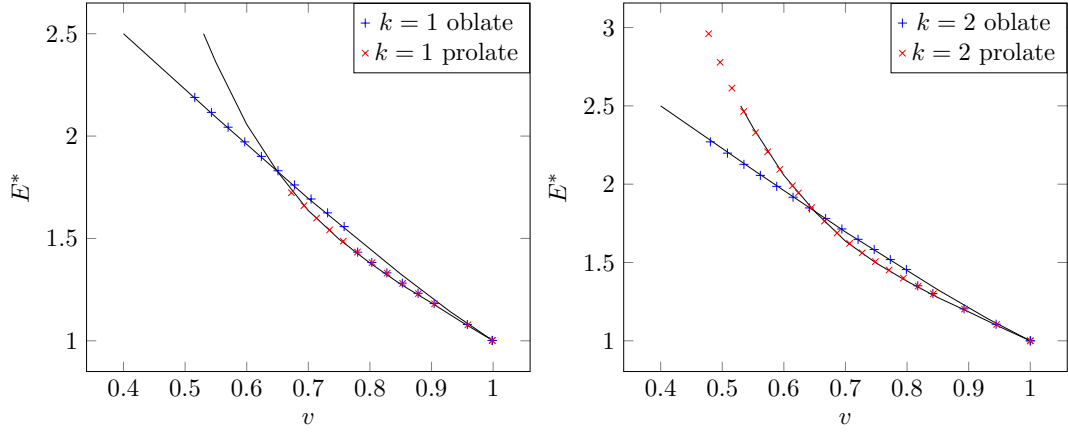


FIGURE 6.6. Results of equilibrium shapes for polynomial orders $k = 1$ (left) and $k = 2$ (right) for prolate and oblate shapes subjected to different volume constraints.

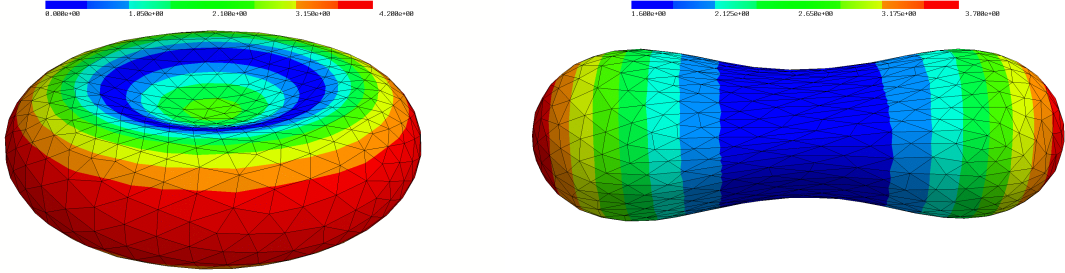


FIGURE 6.7. Characteristic solutions for oblate (left) and prolate (right) branch (red blood cell, dumbbell) with polynomial order $k = 1$, and $v = 0.597$ and $v = 0.713$, respectively.

The results depicted in Figure 6.6 (left) are in good agreement with the theoretical branches, see Figure 6.7 for the characteristic solutions for the oblate and prolate branches.

With the oblate initial shape we were able to converge towards the unstable oblate branch for $0.652 < v < 0.775$, however, for larger reduced volume v after a longer computation time the oblate shape changes significantly converging to a shape on the prolate branch. For the prolate branch leading to the characteristic dumbbell solutions the shape gets heavily stretched for $v < 0.651$ and the mesh regularity becomes ill-shaped leading to an extremely small step-size and the method does not converge anymore.

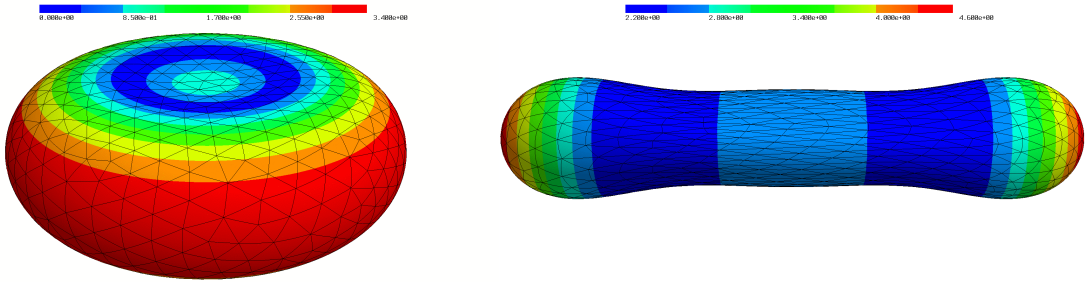


FIGURE 6.8. Oblate and prolate solution with polynomial order $k = 2$ and $v = 0.773$ and $v = 0.594$, respectively.

Next, we redo the same experiments, however, with quadratic instead of linear polynomials and the same meshes are used and curved. Further, we use the improved area preservation procedure described in Section 5.2 solving a Stokes system in each iteration step. As depicted in Figure 6.6 (right) the same qualitative solutions are produced, however, due to the higher polynomial degree the mesh becomes more robust with respect to the mesh quality and thus, we can follow the (unstable) prolate branch longer than for $k = 1$. Further, we are also able to stay longer on the unstable oblate branch for $v > 0.652$, compare Figure 6.8 for two converged shapes.

6.3. Spontaneous curvature H_0 . In this benchmark we consider the same parameters as in the previous section with the only difference of non-zero spontaneous curvature, $H_0 \neq 0$. More precisely, we set $H_0 = 1.2$ and $H_0 = 1.5$ to reproduce the phase diagrams in [47] for these configurations. Further, as we expect strong deformed equilibrium shapes, we directly use quadratic elements, $k = 2$, in combination with the improved area preservation procedure.

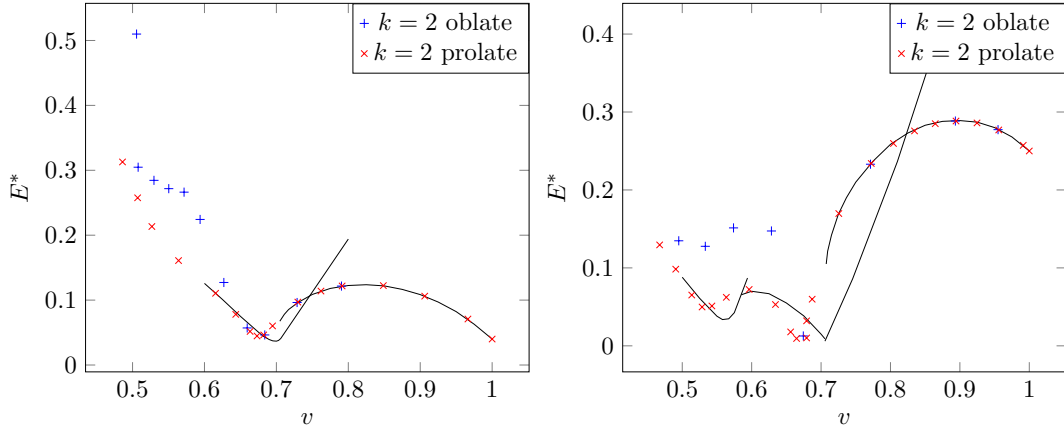


FIGURE 6.9. Results of spontaneous curvature $H_0 = 1.2$ (left) and $H_0 = 1.5$ (right) with polynomial degree $k = 2$.

As depicted in Figure 6.9 (left) we can reproduce the phase diagram for $H_0 = 1.2$ with prolate initial shapes leading to axisymmetric results, compare Figure 6.10. The solutions for $v > 0.7$ form well-shaped dumbbell shapes. At around $v = 0.7$ a bifurcation of branches exists leading to convergence problems. Further, the middle of the dumbbell solutions get heavily narrowed such that the mesh quality becomes critical. For decreasing reduced volume v the dumbbell shapes get longer and for $v < 0.6$ the middle radius increases not being the minimum anymore. For $v < 0.5$ the shape gets heavily stretched and it seems that the local maxima develop. The oblate initial shapes follow the prolate results for $v > 0.65$. In this benchmark, however, we observe that for $v < 0.65$ the unstable red blood cell type shapes converge to a not axisymmetric solution being similar to a dumbbell, but with three ends instead of two, see Figure 6.11. As the results are non axisymmetric this branch could not be analytically computed in [47]. For $v \approx 0.5$ the solution again seems to change. To fulfill the volume constraint the solution is nearly flattened yielding zero mean curvature around its center of gravity. We emphasize that the meshes get deformed heavily and further experiments with improved mesh regularity algorithms have to be performed in future work to investigate this branch. Further, we note that the oblate solutions for $v < 0.65$ did not fully converge to the equilibrate solution due to the distorted meshes, however, reflect the qualitative behavior of the exact solution.

The results shown in Figure 6.9 (right) for $H_0 = 1.5$ also render the phase diagram, however, this configuration is more challenging than the previous one. On the one hand there are two

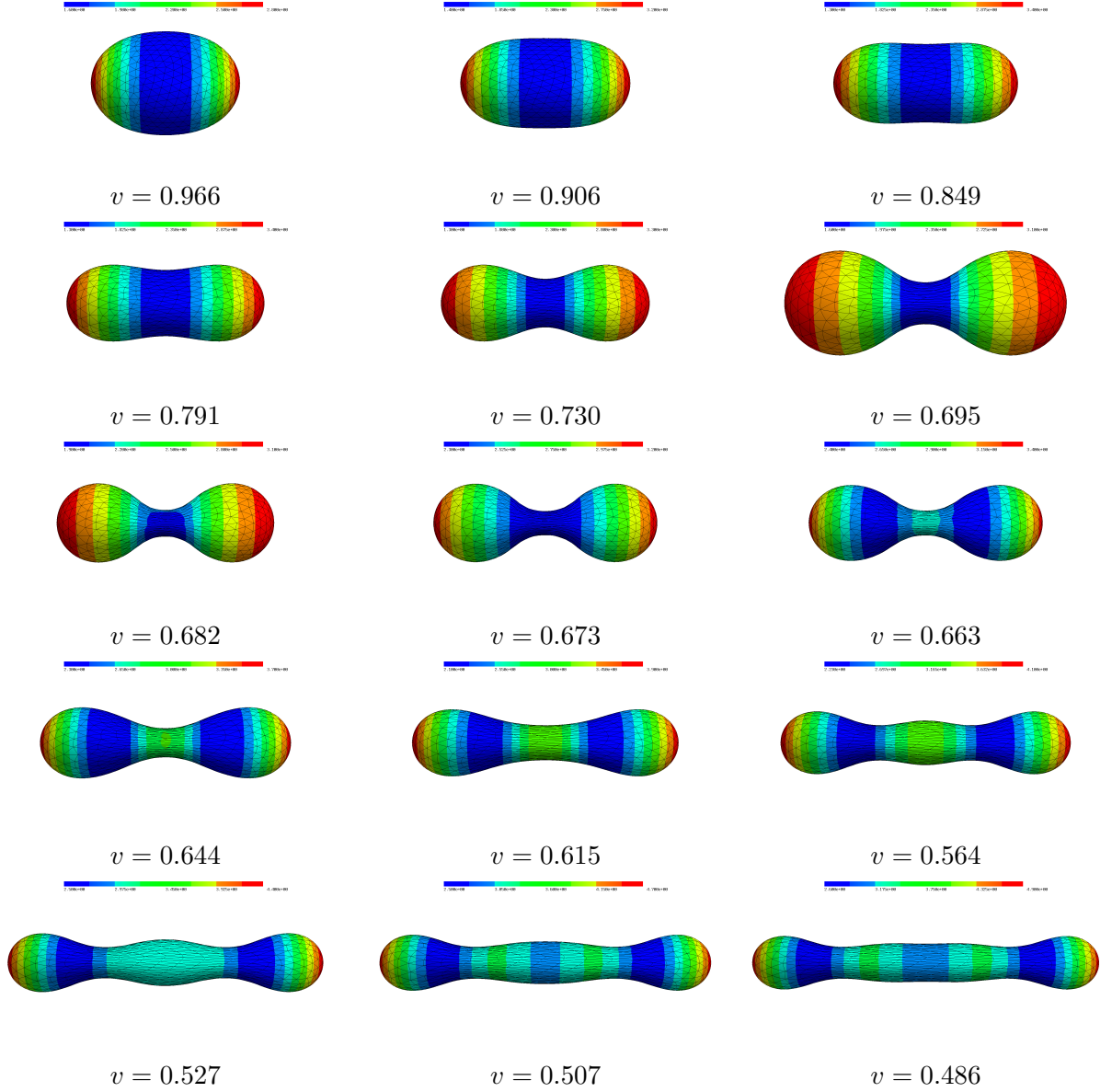


FIGURE 6.10. Prolate shapes for different reduced volumes v with $H_0 = 1.2$ and polynomial order $k = 2$.

bifurcation points at around $v = 0.7$ and $v = 0.58$ and on the other hand the meshes get even more deformed and especially narrowed at the middle. We conclude that remeshing techniques are essentially needed to properly resolve and converge at the bifurcation points. Despite this fact, we observe good agreement with the phase diagram from [47] and obtain the corresponding characteristic solutions comparable to the results in [3], see Figure 6.12. These are again all axisymmetric, whereas the oblate initial shapes again converge to dumbbell solutions with three ends as for $H_0 = 1.2$, compare Figure 6.13. As before the oblate results for $v < 0.65$ did not fully converge, however, definitely indicating that a non axisymmetric oblate branch exists close to them.

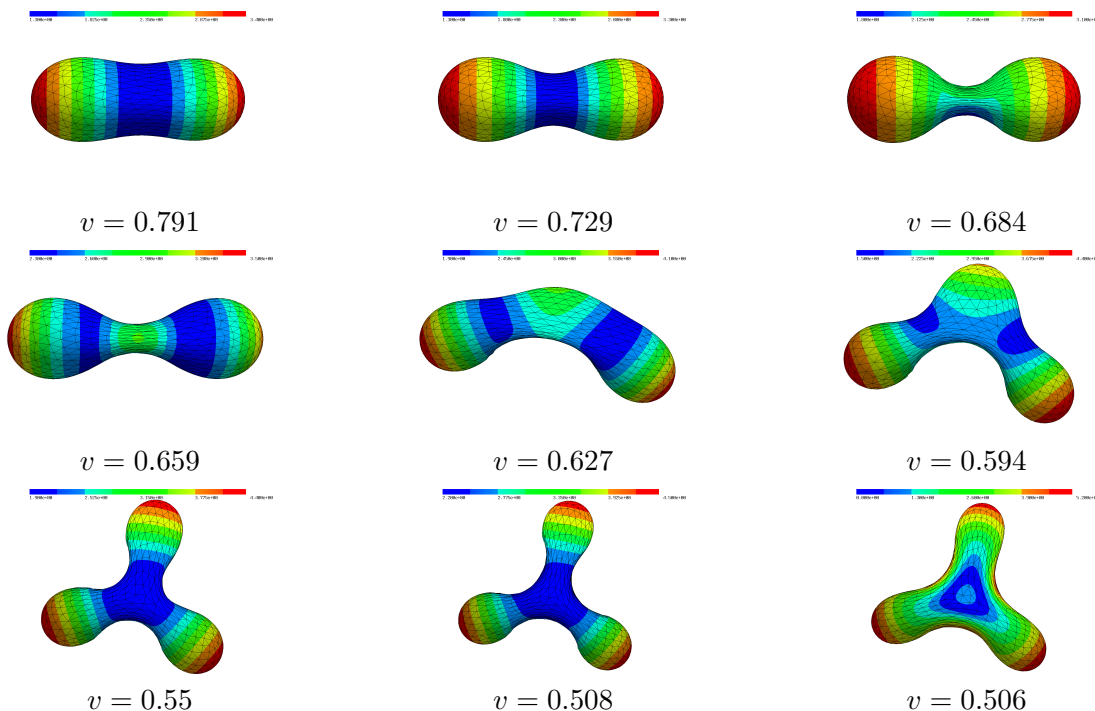


FIGURE 6.11. Oblate shapes for different reduced volumes v with $H_0 = 1.2$ and polynomial order $k = 2$.

CONCLUSION AND FUTURE WORK

In this paper we presented a novel shape optimization method for minimizing the Canham–Helfrich–Evans energy under area and volume constraints based on a lifting of the distributional discrete shape operator. This three-field approach allows for a general formula for the shape derivative independently of the used polynomial order of approximation. A shape gradient optimization procedure has been presented in NGSolve supporting automatic shape differentiation. The performance of the proposed method has been demonstrated on several benchmark examples including curvature computation and spontaneous curvature.

Due to the large deformations of the shapes in specific benchmark configurations, the mesh quality may become poor yielding worse convergence rates or even a termination of the algorithm. Therefore, re-meshing techniques (for arbitrary order of curved geometry) are topic of further research to push forward to more challenging benchmark examples.

DECLARATION OF INTERESTS

The authors declare that they have no known competing financial interests or personal relationships that could have appeared to influence the work reported in this paper.

ACKNOWLEDGEMENTS

Michael Neunteufel acknowledges support from AC2T research GmbH by project 1931712. Joachim Schöberl acknowledges support by the Austrian Science Fund (FWF) project F 65. Kevin Sturm acknowledges support from the Austrian Science Fund (FWF) project P 32911. The authors are also indebted to Ulisse Stefanelli for interesting discussions.

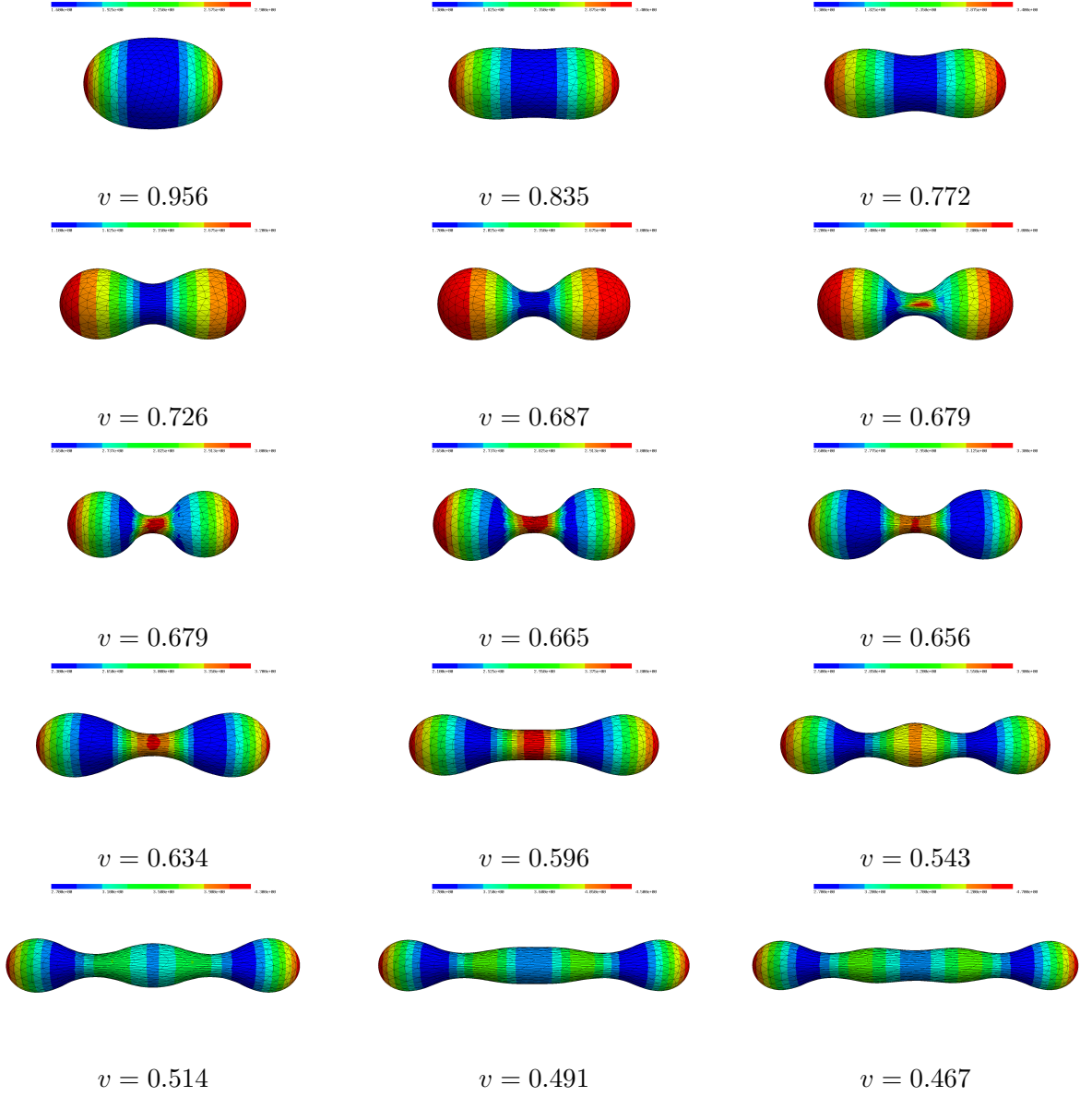


FIGURE 6.12. Prolate shapes for different reduced volumes v with $H_0 = 1.5$ and polynomial order $k = 2$.

APPENDIX A. PROOF OF LEMMA 4.5

For the angle $\angle(a, b) := \arccos(a \cdot b)$, its derivative is given by

$$\frac{d}{dt} \angle(a(t), b(t))|_{t=0} = -\frac{1}{\sqrt{1 - (a(0) \cdot b(0))^2}} \frac{d}{dt} (a(t) \cdot b(t))|_{t=0}.$$

The averaged normal vector $\{\boldsymbol{\nu}\}$ does not depend on the deformation. However, the projection $\mathbf{P}_{\boldsymbol{\tau}^t}^\perp(\cdot)$ (3.17) does. Noting that by construction $\{\boldsymbol{\nu}\} \cdot \boldsymbol{\tau} = 0$ and thus $\mathbf{P}_{\boldsymbol{\tau}}^\perp(\{\boldsymbol{\nu}\}) = \{\boldsymbol{\nu}\}$ there holds

$$\frac{d}{dt} \angle(\boldsymbol{\mu}^t, \mathbf{P}_{\boldsymbol{\tau}^t}^\perp(\{\boldsymbol{\nu}\}))|_{t=0} = -\frac{\frac{d}{dt}(\boldsymbol{\mu}^t \cdot \mathbf{P}_{\boldsymbol{\tau}^t}^\perp(\{\boldsymbol{\nu}\}))|_{t=0}}{\sqrt{1 - (\boldsymbol{\mu} \cdot \{\boldsymbol{\nu}\})^2}}$$

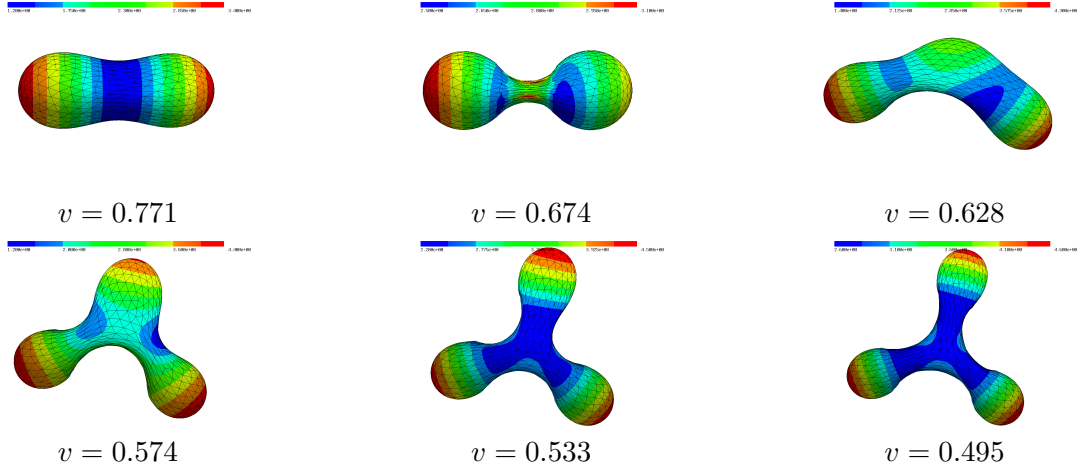


FIGURE 6.13. Oblate shapes for different reduced volumes v with $H_0 = 1.5$ and polynomial order $k = 2$.

and further with the notation $\langle a, b \rangle := a \cdot b$

$$\begin{aligned} \frac{d}{dt} \mathbf{P}_{\tau^t}^\perp(\{\nu\})|_{t=0} &= \frac{-\frac{d}{dt}\{\nu\} \cdot \tau^t \tau^t|_{t=0}}{\|\underbrace{\{\nu\} - \{\nu\} \cdot \tau \tau}_{=0}\|} + \frac{\{\nu\}}{\|\underbrace{\{\nu\} - \{\nu\} \cdot \tau \tau}_{=0}\|^3} \langle \{\nu\}, \frac{d}{dt}\{\nu\} \cdot \tau^t \tau^t|_{t=0} \rangle \\ &= -\frac{d}{dt}\{\nu\} \cdot \tau^t \tau^t|_{t=0} + \{\nu\} \langle \{\nu\}, \frac{d}{dt}\{\nu\} \cdot \tau^t \tau^t|_{t=0} \rangle. \end{aligned}$$

With

$$\begin{aligned} \frac{d}{dt}(\{\nu\} \cdot \tau^t \tau^t)|_{t=0} &= \{\nu\} \cdot \tau (\partial \mathbf{X} \tau - (\partial \mathbf{X} \tau \cdot \tau) \tau) + \{\nu\} \cdot (\partial \mathbf{X} \tau - (\partial \mathbf{X} \tau \cdot \tau) \tau) \tau \\ &= \{\nu\} \cdot \tau (\partial \mathbf{X} \tau) - 2(\partial \mathbf{X} \tau \cdot \tau)(\{\nu\} \cdot \tau) \tau + \{\nu\} \cdot (\partial \mathbf{X} \tau) \tau \\ &= \{\nu\} \cdot (\partial \mathbf{X} \tau) \tau \end{aligned}$$

we get

$$\begin{aligned} \frac{d}{dt} \mathbf{P}_{\tau^t}^\perp(\{\nu\})|_{t=0} &= -\{\nu\} \cdot (\partial \mathbf{X} \tau) \tau + \{\nu\} \langle \{\nu\}, \{\nu\} \cdot (\partial \mathbf{X} \tau) \tau \rangle \\ &= -\{\nu\} \cdot (\partial \mathbf{X} \tau) \tau \end{aligned}$$

and thus with (4.1c), $\mu \cdot \tau = 0$, and $\{\nu\} \cdot \tau = 0$

$$\begin{aligned} \frac{d}{dt}(\mu^t \cdot \mathbf{P}_{\tau^t}^\perp(\{\nu\}))|_{t=0} &= ((\mathbf{I} - \tau \otimes \tau) \partial \mathbf{X} - \partial \mathbf{X}^\top) \mu \cdot \{\nu\} + \mu \cdot (-\{\nu\} \cdot (\partial \mathbf{X} \tau) \tau) \\ &= ((\mathbf{I} - \tau \otimes \tau) \partial \mathbf{X} - \partial \mathbf{X}^\top) \mu \cdot \{\nu\} \\ &= (\partial \mathbf{X} - \partial \mathbf{X}^\top) \mu \cdot \{\nu\} \end{aligned}$$

giving the desired result

$$\frac{d}{dt} \langle \mu^t, \mathbf{P}_{\tau^t}^\perp(\{\nu\}) \rangle|_{t=0} = -\frac{(\partial \mathbf{X} - \partial \mathbf{X}^\top) \mu \cdot \{\nu\}}{\sqrt{1 - (\mu \cdot \{\nu\})^2}}.$$

APPENDIX B. ANGLE EQUIVALENCE

Lemma B.1. *Let $\mathbf{a}, \mathbf{b} \in \mathbf{R}^3$ with $\|\mathbf{a}\| = \|\mathbf{b}\| = 1$. Further let $\mathbf{c} \in \mathbf{R}^3$ with $\|\mathbf{c}\| = 1$ and \mathbf{c} “lies between” \mathbf{a} and \mathbf{b} , i.e., there exists $t \in [0, 1]$ such that $\mathbf{c} \in \text{span}\{t\mathbf{a} + (1-t)\mathbf{b}\}$. Then*

$$\arccos(\mathbf{a} \cdot \mathbf{b}) = \arccos(\mathbf{a} \cdot \mathbf{c}) + \arccos(\mathbf{c} \cdot \mathbf{b}). \quad (\text{B.1})$$

Proof. As $\mathbf{c} \in \text{span}\{\mathbf{a}, \mathbf{b}\}$ we rotate the coordinate system such that all vectors lie w.l.o.g. in the x-y-plane, i.e., $\mathbf{a}, \mathbf{b}, \mathbf{c} \in \mathbf{R}^2$. There holds $\mathbf{a} \cdot \mathbf{b} = \mathcal{R}(a\bar{b})$, where we identified \mathbf{a}, \mathbf{b} with complex numbers, (\cdot) denotes the complex conjugation, and $\mathcal{R}(\cdot)$ the real part. As the vectors are normalized we have

$$a = e^{i\alpha}, \quad b = e^{i\beta}, \quad c = e^{i\gamma}, \quad i^2 = -1, \quad \alpha, \beta, \gamma \in [0, 2\pi).$$

W.l.o.g. assume that $\alpha > \beta$. The condition that \mathbf{c} lies between \mathbf{a} and \mathbf{b} is then equivalent to $\alpha \geq \gamma \geq \beta$. Thus, there holds with $\mathcal{R}(a\bar{b}) = \mathcal{R}(e^{i(\alpha-\beta)}) = \cos(\alpha - \beta)$

$$\arccos(\mathbf{a} \cdot \mathbf{b}) = \arccos(\cos(\alpha - \beta)) \stackrel{\alpha \geq \beta}{=} \alpha - \beta$$

and the right-hand side is

$$\arccos(\mathbf{a} \cdot \mathbf{c}) + \arccos(\mathbf{c} \cdot \mathbf{b}) \stackrel{\alpha \geq \gamma \geq \beta}{=} \alpha - \gamma + \gamma - \beta = \alpha - \beta.$$

□

SUPPLEMENTARY MATERIAL: NUMERICAL SHAPE OPTIMIZATION OF THE
CANHAM-HELFRICH-EVANS BENDING ENERGY

In this supplementary material we present and describe the basic algorithm of our proposed method to solve the Canham–Helfrich–Evans minimization problem including area and volume constraints. For a better presentation we split the code into several snippets. Summing them up an executable file running in NGSolve² [45] is obtained. Note that NumPy³ is required to execute the file. For further details concerning shape optimization in NGSolve we refer to [23].

```

1 from ngsolve import *
2 from netgen.csg import *
3 from netgen.meshing import MeshingStep
4 from math import pi
5 import numpy as np
6
7 autodiff = False # use automatic shape derivative?
8
9 order      = 1      # polynomial order
10 maxh       = 0.2    # mesh-size
11 v          = 0.7    # goal reduced volume
12 H0         = 0      # spontaneous curvature
13
14 kb = 0.01          # bending constant
15 kv = Parameter(1) # penalty for volume
16 kag = Parameter(2) # penalty for global area
17 kal = Parameter(1) # penalty for local area
18
19 xvec = CF( (x,y,z) ) # identity CoefficientFunction
20
21 nsurf = specialcf.normal(3) # outer normal vector
22 tang  = specialcf.tangential(3) # edge tangential vector
23 nel   = Cross(nsurf, tang) # co-normal vector

```

LISTING 1. Include packages and define parameters.

First, we include necessary packages and define several parameters as the used polynomial order and mesh-size. Additionally the identity function as well as the outer normal, edge tangential, and co-normal vector used later are declared.

```

1 geo = CSGeometry()
2 a = 1.1017
3 b = 0.95
4 geo.Add(Ellipsoid(Pnt(0,0,0), Vec(a,0,0), Vec(0,b,0), Vec(0,0,b)))
5 mesh = Mesh(geo.GenerateMesh(maxh=maxh, perfstepsend=MeshingStep.MESHSURFACE))
6 mesh.Curve(order)
7 Draw(mesh)

```

LISTING 2. Define mesh.

In Listing 2 we generate a prolate initial surface shape with given mesh-size and curve it appropriately.

```

1 A0 = Integrate(1, mesh, BND) # initial area
2 V0 = Integrate(1/3*xvec*nsurf, mesh, BND) # initial volume
3 V  = v*4/3*pi*(A0/(4*pi))**(3/2) # goal volume
4
5 At0 = GridFunction(SurfaceL2(mesh, order=0)) # initial local areas
6 At0.vec.FV().NumPy()[:] = Integrate(1, mesh, BND, element_wise=True)

```

²www.ngsolve.org

³www.numpy.org

```

7
8 At = GridFunction(SurfaceL2(mesh, order=0))
9 At.vec.data = At0.vec      # initialize current local areas
10 A_cur = Parameter(A0)      # initialize current area
11 V_cur = Parameter(V0)      # initialize current volume

```

LISTING 3. Preparation for are and volume constraint.

Next, we compute the initial area and enclosed volume of the mesh and define the goal volume by means of the reduced volume parameter. Further, the area of each triangle is stored for the local area stabilization constraint. The involved `SurfaceL2` space of order=0 consists of a constant value per surface element, which is stored in the `GridFunction` object. If required the `GridFunction` can be drawn visualizing the local areas.

```

1 # compute normalized Canham–Helfrich–Evans energy
2 def Energy(kappa, gfset):
3     mesh.SetDeformation(gfset)
4     energy = Integrate(2*kb*(1/2*kappa-H0)**2, mesh, BND)
5     mesh.UnsetDeformation()
6     return energy/(8*pi*kb)
7
8 # compute costs w.r.t. bending energy and area/volume constraints
9 def Cost(kappa):
10     # compute current areas, volume, and bending energy
11     A_cur.Set(Integrate(1, mesh, BND))
12     At.vec.FV().NumPy[:] = Integrate(1, mesh, BND, element_wise=True)
13     V_cur.Set(1/3*Integrate(xvec*nsurf, mesh, BND))
14     bending = Integrate(2*kb*(1/2*kappa-H0)**2, mesh, BND)
15
16     constr_At = kal.Get()*(np.square(At.vec.FV().NumPy()-At0.vec.FV().NumPy())/
17                               At0.vec.FV().NumPy()).sum()
18     constraint = kag.Get()*(A_cur.Get()-A0)**2/A0 + kv.Get()*(V_cur.Get()-V)**2/V
19     + constr_At
20
21     return bending + constraint
22
23 # return shape derivative of Cost functional
24 def CostDiff(kappa, PSI):
25     if autodiff: # automatic shape derivative
26         bending = (2*kb*(1/2*kappa-H0)**2*ds).DiffShape(PSI)
27         constr = (2*(kag*(A_cur-A0)/A0 + kal*(At-At0)/At0 + kv*(V_cur-V)/V/3*xvec*
28                  nsurf)*ds).DiffShape(PSI)
29     else: # manual shape derivative
30         tangdet = div(PSI).Trace() # surface divergence
31         bending = 2*kb*tangdet*(1/2*kappa-H0)**2*ds
32         constr = 2*(kag*(A_cur-A0)/A0*tangdet + kv*(V_cur-V)/V*PSI*nsurf + kal*(At
33               -At0)/At0*tangdet)*ds
34     return bending + constr

```

LISTING 4. Energy, Cost, and CostDiff auxiliary function.

The function `Energy` computes the normalized Canham–Helfrich–Evans bending energy. Additionally to the curvature κ also a `GridFunction` object storing the current displacement information of the mesh is handed over. With the method `SetDeformation` of the mesh all integration procedures are performed as if we would consider the deformed mesh according to the displacement until the `UnsetDeformation` command is used.

The `Cost` function computes the current Canham–Helfrich–Evans bending energy together with the area and volume constraints. Note, that we use NumPy to avoid slow Python for-loops.

Next, we need the shape derivative of the cost functional in direction Ψ defined later. We can

either use the build-in automatic shape differentiation procedure denoted by `DiffShape(PSI)` [23] or by manually computing the derivatives. Note that the `ds` object indicates that the integration will be performed on the surface.

```

1 # return equation
2 def Equation(kappa, sigma, nav):
3     return (kappa*sigma + Trace(Grad(nsurf))*sigma)*ds + (pi/2-acos(nel*nav))*
        sigma*ds(element_boundary=True)
4
5 # return shape derivative of equation
6 def EquationDiff(kappa, sigma, nav, PSI):
7     if autodiff: # automatic shape derivative
8         return Equation(kappa, sigma, nav).DiffShape(PSI)
9
10 # manual shape derivative
11 tangdet = div(PSI).Trace()
12 return (tangdet*(kappa*sigma + Trace(Grad(nsurf))*sigma) + ((Grad(PSI).Trace()
    *Grad(sigma))*nsurf - Trace(Grad(PSI).Trace().trans*Grad(nsurf))*sigma))*
    ds + (((Grad(PSI).Trace()*tang)*tang*(pi/2-acos(nel*nav)) + 1/sqrt(1-
    InnerProduct(nav,nel)**2))*((Grad(PSI).Trace() - Grad(PSI).Trace().trans)*
    nel)*nav)*sigma - (Grad(PSI).Trace()*nel)*nsurf*sigma)*ds(element_boundary=
    True)

```

LISTING 5. Equation and EquationDiff auxiliary function.

In Listing 5 we define the equation of the state problem, where the distributional curvature gets lifted to the auxiliary curvature field κ . For the needed shape derivative we again can directly differentiate it. The analytical computations presented in the paper are quite involved, however, manageable.

```

1 VEC = VectorH1(mesh, order=order) # vector-Lagrange finite element space
2 PHI, PSI = VEC.TnT() # trial- and testfunction
3
4 gfX = GridFunction(VEC) # store shape gradient
5 gfset = GridFunction(VEC) # store current displacement
6
7 fes = H1(mesh, order=order) # Lagrange finite element space
8 kappa, sigma = fes.TnT() # trial- and testfunction
9
10 gfkappa = GridFunction(fes) # store curvature (state)
11 gfsigma = GridFunction(fes) # store moments (adjoint state)
12
13 # space for averaging normal vector
14 fesfacet = VectorFacetSurface(mesh, order=order-1)
15 gfh = GridFunction(fesfacet) # store the averaged normal vector
16 nav = Normalize(CF( gfh.components )) # normalize averaged normal vector
17
18 # left-hand side for solving (adjoint) state problem
19 a = BilinearForm(fes, symmetric=True)
20 a += kappa*sigma*ds
21 a.Assemble() # assemble and invert as preparation
22 inva = a.mat.Inverse(freedofs=fes.FreeDofs(), inverse="sparsecholesky")
23
24 # right-hand side for state problem (curvature)
25 fa = LinearForm(fes)
26 fa += -Trace(Grad(nsurf))*sigma*ds - (pi/2-acos(nel*nav))*sigma*ds(
    element_boundary=True)
27
28 # right-hand side for adjoint state problem
29 dCostdu = LinearForm(fes)
30 dCostdu += 2*kb*(1/2*gfkappa-H0)*sigma*ds

```

```

31
32 # left-hand side for shape optimization gradient method
33 aX = BilinearForm(VEC, symmetric=True)
34 aX += (InnerProduct(Grad(PHI).Trace(), Grad(PHI).Trace()) + 1e-10*PHI*PSI)*ds
35 aX.Assemble() # assemble and invert as preparation
36 invaX = aX.mat.Inverse(VEC.FreeDofs(), inverse="sparsecholesky")
37
38 # right-hand side for shape optimization gradient method
39 fX = LinearForm(VEC)
40 fX += CostDiff(gfkappa, PSI).Compile()
41 fX += EquationDiff(gfkappa, gfsigma, nav, PSI).Compile()

```

LISTING 6. (Bi-)Linear forms for (adjoint) state and shape gradient problem.

After having defined the important functions we can focus on the solving algorithm. For the displacement field and the shape gradient we use a vector-valued Lagrange finite element space and define the symbolic trial- and testfunction objects Φ and Ψ . The shape gradient and displacement field themselves get stored as a **GridFunction** object of the H^1 -conforming finite element space.

The independent curvature field κ as well as the Lagrange multiplier (adjoint state) σ are discretized by scalar Lagrange elements and get stored in the corresponding **GridFunctions**. To compute the used averaged normal vector a **SurfaceVectorFacet** finite element space is used living only on the edges (the skeleton) of the triangulation. The corresponding **GridFunction** needs to be normalized to measure the correct angle. As discussed in the paper we directly neglected the projection operator $\mathbf{P}_\tau^\perp(\cdot)$ to reduce the expressions gaining performance, which, however, could be implemented with the following line.

```

1 nav = Normalize( CF( gfh.components ) - (tang*CF( gfh.components ))*tang )

```

LISTING 7. Projected averaged normal vector.

To solve the state and adjoint state problem a mass matrix is assembled and inverted with the build-in “sparsecholesky” solver. The right-hand side for the state problem gets represented by the **LinearForm** **fa**, which is written completely symbolically. We note that $\dots *ds(\text{element_boundary}=\text{True})$ corresponds to the integral $\sum_{T \in \mathcal{T}_h} \int_{\partial T} \dots d\gamma$. the right-hand side of the adjoint state problem is given by the variation of the Canham–Helfrich–Evans energy with respect to the curvature κ .

For the shape optimization gradient method we define, assemble, and invert the (regularized) H^1 -scalar product. The right-hand side is given by the shape derivative of the state equation as well as the cost functional. Note that the **Compile()** statement optimizes the internally generated expression tree of symbolic expressions to gain evaluation performance.

```

1 def solvePDE():
2     # average current normal vector
3     gfh.Set(nsurf, dual=True, definedon=mesh.Boundaries(".*"))
4     # solve adjoint and state equation
5     a.Assemble()
6     fa.Assemble()
7     inva.Update()
8     gfkappa.vec.data = inva*fa.vec
9     dCostdu.Assemble()
10    gfsigma.vec.data = -inva*dCostdu.vec
11    return

```

LISTING 8. Solve current (adjoint) state problem.

As we need to solve the (adjoint) state problem in every optimization step, we summarize them in Listing 8. First, the new normal vector is averaged and then the problems for κ and σ are solved.

```

1 solvePDE()
2 Draw(gfX, mesh, "gfX")
3 Draw(gfsigma, mesh, "adjoint")
4 Draw(gfkappa, mesh, "state")
5 Draw(gfset, mesh, "displacement")
6 Draw(Norm(0.5*gfX), mesh, "mean")
7 SetVisualization(deformation=True)
8
9 iter_max          = 1000    # maximal number of optimization steps
10 scale_init       = 0.025   # initial step-size
11 scale_max        = 0.1     # maximal step-size
12 scaleIncreaseFactor = 1.00  # increasing factor after accepted step
13 tol_scale        = 1e-11   # tolerance for minimal step-size
14 tol_gfX          = 1e-12   # tolerance for shape gradient
15 tol_J            = 1e-10   # tolerance for costs
16 normGFX_start    = None    # store initial shape gradient
17
18 isConverged = False
19 Jold        = 0            # store previous costs
20 gfsettmp    = GridFunction(VEC) # store temporary mesh displacement

```

LISTING 9. Draw fields and optimization parameters.

In Listing 9 all quantities are drawn for visualization and the mesh will be visually deformed to the current shape by the `SetVisualization(deformation=True)` command. Then, several self-explaining optimization parameters are defined.

```

1 with TaskManager():
2     solvePDE()
3     Jnew = Cost(gfkappa)
4     Jold = Jnew
5
6     print("it init", 'cost', Jnew)
7     scale = scale_init
8
9     for k in range(iter_max):
10         # solve (adjoint) state problem and prepare shape derivative
11         mesh.SetDeformation(gfset)
12         solvePDE()
13         aX.Assemble()
14         fX.Assemble()
15         mesh.UnsetDeformation()
16
17         invaX.Update()
18         gfX.vec.data = invaX * fX.vec # next shape gradient
19
20         currentNormGFX = Norm(gfX.vec)
21         if k == 0: normGFX_start = currentNormGFX
22
23         while True: # line-search
24             if scale < tol_scale or currentNormGFX < normGFX_start*tol_gfX or Jnew <
25                 tol_J: # converged?
26                 isConverged = True
27                 break
28
29             # guess for next mesh displacement
30             gfsettmp.vec.data = gfset.vec - scale * gfX.vec
31
32             mesh.SetDeformation(gfsettmp)
33             solvePDE()
34             Jnew = Cost(gfkappa)

```



```

34     mesh.UnsetDeformation()
35
36     if Jnew <= Jold: # accept step?
37         Jold = Jnew
38         print("-----it", k, 'scale', scale, 'cost', Jnew )
39         gfset.vec.data = gfsettmp.vec
40         scale = min(scale_max, scale*scaleIncreaseFactor)
41         break
42     else: # if not, reduce step-size
43         scale = scale / 2
44
45     print("-----||gfX||", currentNormGFX)
46
47     Redraw() # redraw solutions
48
49     if isConverged:
50         print("converged with J = ", Jnew, ", ||gfX||=", currentNormGFX, ", scale
51             = ", scale)
52         break

```

LISTING 10. Shape optimization gradient method loop.

Finally, the shape gradient Algorithm 5.1 in the paper is presented in Listing 10. First, we activate the build-in **TaskManager** to perform the following assembling and inversion processes in (thread-)parallel, solve the (adjoint) state problem on the initial shape and evaluate the cost function. In every optimization step we re-compute the (adjoint) state problem as well as the next shape gradient on the current configuration of the mesh. Therefore, analogously as in Listing 4 in the **Energy** function, we use the **SetDeformation** method, where the **GridFunction** object **gfset** is used as input having stored the displacement information how the initial mesh has to be deformed to obtain the current shape. Next, a line-search is performed to guarantee that the final gradient step non-increases the cost functional. Therefore, the temporary object **gfsettmp** saves the previous displacement plus a scaled gradient step with the step-size parameter **size**. After computing the cost functional on the temporary configuration the decrease of the cost functional is checked. If accepted, the step-size is increased by an factor, otherwise the step-size gets halved and a gradient step with the reduced size is tried until the cost functional decreases or the step-size becomes too small yielding a break down of the algorithm.

```

1  # compute final area, volume, reduced volume, cost, and energy
2  mesh.SetDeformation(gfset)
3  Vnew = Integrate(1/3*xvec*nsurf, mesh, BND)
4  Anew = Integrate(1, mesh, BND)
5  vnew = Vnew/(4/3*pi*(Anew/(4*pi))**(3/2))
6  cost = Cost(gfkappa)
7  mesh.UnsetDeformation()
8
9  print("cost    = ", cost)
10 print("energy = ", Energy(gfkappa, gfset))
11 print("Vnew   = ", Vnew)
12 print("Anew   = ", Anew)
13 print("vnew   = ", vnew)

```

LISTING 11. Postprocessing.

After the algorithm determined, the quantities as area and volume are updated. Note that the final reduced volume v_{new} does not necessarily need to coincide with the goal reduced volume v from Listing 1 as the penalty method for the area and volume constraints is used.

REFERENCES

- [1] BARRETT, J. W., GARCKE, H., AND NÜRNBERG, R. Parametric approximation of Willmore flow and related geometric evolution equations. *SIAM Journal on Scientific Computing* 31, 1 (2008), 225–253.
- [2] BAUER, U., POLTHIER, K., AND WARDETZKY, M. Uniform convergence of discrete curvatures from nets of curvature lines. *Discrete & Computational Geometry* 43, 4 (2010), 798–823.
- [3] BIAN, X., LITVINOV, S., AND KOUMOUTSAKOS, P. Bending models of lipid bilayer membranes: Spontaneous curvature and area-difference elasticity. *Computer Methods in Applied Mechanics and Engineering* 359 (2020), 112758.
- [4] BIBEN, T., FARUTIN, A., AND MISBAH, C. Three-dimensional vesicles under shear flow: Numerical study of dynamics and phase diagram. *Phys. Rev. E* 83 (2011), 031921.
- [5] BLAUTH, S. Nonlinear conjugate gradient methods for PDE constrained shape optimization based on Steklov–Poincaré-type metrics. *SIAM J. Optim.* 31, 3 (2021), 1658–1689.
- [6] BOEDER, G., LEONETTI, M., AND JAEGER, M. 3D vesicle dynamics simulations with a linearly triangulated surface. *Journal of Computational Physics* 230, 4 (2011), 1020–1034.
- [7] BONITO, A., NOCHETTO, R. H., AND PAULETTI, M. S. Geometrically consistent mesh modification. *SIAM Journal on Numerical Analysis* 48, 5 (2010), 1877–1899.
- [8] BONITO, A., NOCHETTO, R. H., AND SEBASTIAN PAULETTI, M. Parametric FEM for geometric biomembranes. *Journal of Computational Physics* 229, 9 (2010), 3171–3188.
- [9] CANHAM, P. B. The minimum energy of bending as a possible explanation of the biconcave shape of the human red blood cell. *Journal of Theoretical Biology* 26, 1 (1970), 61–81.
- [10] CHICCO-RUIZ, A., MORIN, P., AND PAULETTI, M. S. The shape derivative of the Gauss curvature, 2017.
- [11] COMODI, M. I. The Hellan–Herrmann–Johnson method: Some new error estimates and postprocessing. *Mathematics of Computation* 52, 185 (1989), 17–29.
- [12] DELFOUR, M. C., AND ZOLÉSIO, J.-P. *Shapes and Geometries. Metrics, Analysis, Differential Calculus, and Optimization*, second ed. Society for Industrial and Applied Mathematics (SIAM), Philadelphia, 2011.
- [13] DEMKOWICZ, L. Projection-based interpolation. *ICES Report* 4, 3 (2004), 1–22.
- [14] DEULING, H.J., AND HELFRICH, W. The curvature elasticity of fluid membranes : A catalogue of vesicle shapes. *J. Phys. France* 37, 11 (1976), 1335–1345.
- [15] DOĞAN, G., AND NOCHETTO, R. H. First variation of the general curvature-dependent surface energy. *ESAIM: Mathematical Modelling and Numerical Analysis* 46, 1 (2012), 59–79.
- [16] DOHRMANN, C. R., AND BOCHEV, P. B. A stabilized finite element method for the stokes problem based on polynomial pressure projections. *International Journal for Numerical Methods in Fluids* 46, 2 (2004), 183–201.
- [17] DU, Q., LIU, C., AND WANG, X. A phase field approach in the numerical study of the elastic bending energy for vesicle membranes. *Journal of Computational Physics* 198, 2 (2004), 450–468.
- [18] DZIUK, G. An algorithm for evolutionary surfaces. *Numerische Mathematik* 58, 1 (1990), 603–611.
- [19] DZIUK, G., AND ELLIOTT, C. M. Finite element methods for surface PDEs. *Acta Numerica* 22 (2013), 289–396.
- [20] ELLIOTT, C. M., STINNER, B., AND VENKATARAMAN, C. Modelling cell motility and chemotaxis with evolving surface finite elements. *Journal of The Royal Society Interface* 9, 76 (2012), 3027–3044.
- [21] EVANS, E. Bending resistance and chemically induced moments in membrane bilayers. *Biophysical Journal* 14, 12 (1974), 923–931.
- [22] FARUTIN, A., BIBEN, T., AND MISBAH, C. 3D numerical simulations of vesicle and inextensible capsule dynamics. *Journal of Computational Physics* 275 (2014), 539–568.
- [23] GANGL, P., STURM, K., NEUNTEUFEL, M., AND SCHÖBERL, J. Fully and semi-automated shape differentiation in NGSolve. *Structural and Multidisciplinary Optimization* 63, 3 (2021), 1579–1579.
- [24] GRINSPUN, E., GINGOLD, Y., REISMAN, J., AND ZORIN, D. Computing discrete shape operators on general meshes. *Computer Graphics Forum* 25, 3 (2006), 547–556.
- [25] GUCKENBERGER, A., AND GEKLE, S. Theory and algorithms to compute Helfrich bending forces: a review. *Journal of Physics: Condensed Matter* 29, 20 (2017), 203001.
- [26] HELFRICH, W. Elastic properties of lipid bilayers: Theory and possible experiments. *Zeitschrift für Naturforschung C* 28, 11-12 (1973), 693–703.
- [27] IGLESIAS, J. A., STURM, K., AND WECHSUNG, F. Two-dimensional shape optimization with nearly conformal transformations. *SIAM Journal on Scientific Computing* 40, 6 (2018), A3807–A3830.
- [28] KOVÁCS, B., LI, B., AND LUBICH, C. A convergent evolving finite element algorithm for mean curvature flow of closed surfaces. *Numerische Mathematik* 143, 4 (2019), 797–853.
- [29] KOVÁCS, B., LI, B., AND LUBICH, C. A convergent evolving finite element algorithm for Willmore flow of closed surfaces, 2020.

- [30] LAADHARI, A., MISBAH, C., AND SARAMITO, P. On the equilibrium equation for a generalized biological membrane energy by using a shape optimization approach. *Physica D: Nonlinear Phenomena* 239, 16 (2010), 1567–1572.
- [31] LAADHARI, A., SARAMITO, P., AND MISBAH, C. Computing the dynamics of biomembranes by combining conservative level set and adaptive finite element methods. *Journal of Computational Physics* 263 (2014), 328–352.
- [32] LAURAIN, A., AND STURM, K. Distributed shape derivative via averaged adjoint method and applications. *ESAIM: M2AN* 50, 4 (2016), 1241–1267.
- [33] LENOIR, M. Optimal isoparametric finite elements and error estimates for domains involving curved boundaries. *SIAM Journal on Numerical Analysis* 23, 3 (1986), 562–580.
- [34] MA, L., AND KLUG, W. S. Viscous regularization and r-adaptive remeshing for finite element analysis of lipid membrane mechanics. *Journal of Computational Physics* 227, 11 (2008), 5816–5835.
- [35] MAITRE, E., MISBAH, C., PEYLA, P., AND RAOULT, A. Comparison between advected-field and level-set methods in the study of vesicle dynamics. *Physica D: Nonlinear Phenomena* 241, 13 (2012), 1146–1157.
- [36] MEYER, M., DESBRUN, M., SCHRÖDER, P., AND BARR, A. H. Discrete differential-geometry operators for triangulated 2-manifolds. In *Visualization and Mathematics III* (Berlin, Heidelberg, 2003), H.-C. Hege and K. Polthier, Eds., Springer Berlin Heidelberg, pp. 35–57.
- [37] MOHANDAS, N., AND EVANS, E. Mechanical properties of the red cell membrane in relation to molecular structure and genetic defects. *Annual Review of Biophysics and Biomolecular Structure* 23, 1 (1994), 787–818.
- [38] NEUNTEUFEL, M. *Mixed Finite Element Methods for Nonlinear Continuum Mechanics and Shells*. PhD thesis, TU Wien, 2021.
- [39] NEUNTEUFEL, M., AND SCHÖBERL, J. The Hellan–Herrmann–Johnson method for nonlinear shells. *Computers & Structures* 225 (2019), 106109.
- [40] NOCEDAL, J., AND WRIGHT, S. J. *Numerical Optimization*, 2 ed. Springer, New York, 2006.
- [41] PAULETTI, M. S. *Parametric AFEM for geometric evolution equation and coupled fluid-membrane interaction*. PhD thesis, University of Maryland, College Park, 2008.
- [42] POZRIKIDIS, C. *Boundary Integral and Singularity Methods for Linearized Viscous Flow*. Cambridge Texts in Applied Mathematics. Cambridge University Press, 1992.
- [43] SAUER, R. A., DUONG, T. X., MANDADAPU, K. K., AND STEIGMANN, D. J. A stabilized finite element formulation for liquid shells and its application to lipid bilayers. *Journal of Computational Physics* 330 (2017), 436–466.
- [44] SCHÖBERL, J. NETGEN an advancing front 2D/3D-mesh generator based on abstract rules. *Computing and visualization in science* 1, 1 (1997), 41–52.
- [45] SCHÖBERL, J. C++11 implementation of finite elements in NGSolve. *Institute for Analysis and Scientific Computing, Vienna University of Technology* (2014).
- [46] SCHULZ, V. H., SIEBENBORN, M., AND WELKER, K. Efficient PDE constrained shape optimization based on Steklov–Poincaré-type metrics. *SIAM J. Optim.* 26, 4 (2016), 2800–2819.
- [47] SEIFERT, U., BERNDL, K., AND LIPOWSKY, R. Shape transformations of vesicles: Phase diagram for spontaneous- curvature and bilayer-coupling models. *Phys. Rev. A* 44 (1991), 1182–1202.
- [48] SEOL, Y., HU, W.-F., KIM, Y., AND LAI, M.-C. An immersed boundary method for simulating vesicle dynamics in three dimensions. *Journal of Computational Physics* 322 (2016), 125–141.
- [49] SINWEL, A., AND SCHÖBERL, J. Tangential-displacement and normal-normal-stress continuous mixed finite elements for elasticity. *Math. Models Methods Appl. Sci.* 21, 8 (2011), 1761–1782.
- [50] SOKOLOWSKI, J., AND ZOLÉSIO, J.-P. *Introduction to Shape Optimization: Shape Sensitivity Analysis*, 1 ed. Springer Berlin Heidelberg, Berlin, Heidelberg, 1992.
- [51] STEINER, J. Über parallele Flächen. *Monatsber. Preuss. Akad. Wiss* 2 (1840), 114–118.
- [52] TORRES-SÁNCHEZ, A., MILLÁN, D., AND ARROYO, M. Modelling fluid deformable surfaces with an emphasis on biological interfaces. *Journal of Fluid Mechanics* 872 (2019), 218–271.
- [53] VEERAPANENI, S. K., RAHIMIAN, A., BIROS, G., AND ZORIN, D. A fast algorithm for simulating vesicle flows in three dimensions. *Journal of Computational Physics* 230, 14 (2011), 5610–5634.
- [54] WALKER, S. W. *The Shapes of Things*. Society for Industrial and Applied Mathematics, Philadelphia, 2015.
- [55] WARDETZKY, M., BERGOU, M., HARMON, D., ZORIN, D., AND GRINSPUN, E. Discrete quadratic curvature energies. *Computer Aided Geometric Design* 24, 8 (2007), 499–518.

(Michael Neunteufel) INSTITUTE FOR ANALYSIS AND SCIENTIFIC COMPUTING, TU WIEN, WIEDNER HAUPT-STRASSE 8-10, 1040 WIEN, AUSTRIA.

Email address: `michael.neunteufel@tuwien.ac.at`

URL: https://www.asc.tuwien.ac.at/~schoeberl/wiki/index.php/Michael_Neunteufel

(Joachim Schöberl) INSTITUTE FOR ANALYSIS AND SCIENTIFIC COMPUTING, TU WIEN, WIEDNER HAUPT-STRASSE 8-10, 1040 WIEN, AUSTRIA.

Email address: `joachim.schoeberl@tuwien.ac.at`

URL: https://www.asc.tuwien.ac.at/~schoeberl/wiki/index.php/Joachim_Schöberl

(Kevin Sturm) INSTITUTE FOR ANALYSIS AND SCIENTIFIC COMPUTING, TU WIEN, WIEDNER HAUPT-STRASSE 8-10, 1040 WIEN, AUSTRIA.

Email address: `kevin.sturm@tuwien.ac.at`

URL: <https://www.asc.tuwien.ac.at/sturm/>